This is the Accepted version of the manuscript: Giaccio, B., Marino, G., Marra, F., Monaco, L., Pereira, A., Zanchetta, G., Gaeta, M., Leicher, N., Nomade, S., Palladino, D.M., Sottili, G., Guillou, H. & Scao, V. 2021. Tephrochronological constraints on the timing and nature of sea-level change prior to and during glacial termination V. Quaternary Science Reviews, vol. 263, 106976.

Tephrochronological constraints on the timing and nature of sea-level change prior to and during glacial termination V

Biagio Giaccio [a, b], Gianluca Marino [c, d], Fabrizio Marra [b, *], Lorenzo Monaco [e], Alison Pereira [f], Giovanni Zanchetta [g], Mario Gaeta [e], Niklas Leicher [h], Sébastien Nomade [i], Danilo M. Palladino [e], Gianluca Sottili [e], Hervé Guillou [i], Vincent Scao [i]

[a] Istituto di Geologia Ambientale e Geoingegneria, CNR, Roma, Italy
[b] Istituto Nazionale di Geofisica e Vulcanologia, Rome, Italy
[c] Centro de Investigación Marina, GEOMA, Palaeoclimatology Lab, Universidade de Vigo, Vigo, Spain
[d] Research School of Earth Sciences, The Australian National University, Canberra, Australian Capital Territory, Australia
[e] Sapienza Università di Roma, Dipartimento di Scienze della Terra, Piazzale Aldo Moro 5, 00185, Roma, Italy
[f] UMR 8148, Laboratoire GEOPS, Université Paris-Saclay, F-914505 Orsay, France
[g] Dipartimento di Scienze della Terra, University of Pisa, Pisa, Italy
[h] Institute of Geology and Mineralogy, University of Cologne, Cologne, Germany
[i] Laboratoire des Sciences du Climat et de l'Environnement, LSCE/IPSL, CEA-CNRS-UVSQ, Université Paris-Saclay, F-91191, Gif-sur-Yvette, France

a r t i c l e i n f o

Article history:
Received 6 August 2020
Received in revised form
12 April 2021
Accepted 24 April 2021
Available online 18 May 2021

Handling Editor: I. Hendy

Keywords:
MIS 12 to MIS 11 transition
Aggradational successions
Meltwater pulse events
Heinrich-like events
Middle pleistocene
$^{40}Ar/^{39}Ar$ geochronology

a b s t r a c t

Glacial-interglacial variations in ice volume and sea level are essential components of the Pleistocene global climate evolution. Deciphering the timing of change of these key climate parameters with respect to the insolation forcing is central to understanding the processes controlling glacial terminations. Here we exploit the sensitivity of the Paleo Tiber River (central Italy) to sea-level forced changes in the base level and the frequent occurrence of datable tephra layers in its sedimentary successions to reconstruct the timing of the relative sea-level (RSL) change between 450 and 403 ka, i.e., across the glacial termination (T-V) that marks the transition between Marine Isotope Stage (MIS) 12 and MIS 11. The analysis hinges on new stratigraphic data, tephra geochemical fingerprinting, and $^{40}Ar/^{39}Ar$ dating from a fluvial section that represents the inland counterpart of the near mouth, coastal aggradational successions of the San Paolo Formation (SPF). Tephra correlation indicates that the morpho-stratigraphic record of the inland section is as sensitive to the sea-level change as its coastal counterparts, which makes it ideal to complement previous RSL reconstructions from the Tiber River catchment basin, thereby providing a more detailed picture of the sea-level history across T-V. Combined sedimentological and morphological proxies of the composed inland-coastal SPF record document the occurrence of two phases of relatively rapid sea-level rise, here interpreted as meltwater pulse (MWP) events. The earlier MWP occurred between ~450 and ~445 ka and matches a relatively minor episode of the sea-level rise documented in an existing RSL record, while the younger MWP at ~430 ka corresponds to the high amplitude sea-level rise that marks T-V. We find that both MWPs coincide with episodes of ice-rafted debris deposition in the North Atlantic (Heinrich-like events) and with attendant Southern Hemisphere warming, plausibly associated with the bipolar seesaw.

1. Introduction

Glacial Marine Isotope Stage 12 (MIS 12) and the ensuing glacial termination (Termination V, T-V) that marks the transition into the long-lasting interglacial climate conditions of MIS 11 represent a fundamental step in the evolution of the Pleistocene glacial-interglacial cycles (e.g., Droxler et al., 2003). The glacial maximum of MIS 12 constitutes the culmination of the stepwise intensification of glacial conditions (greater ice volume, lower atmospheric CO_2 concentrations) that accompanied the Middle Pleistocene Transition and the attendant emergence of the long, high-amplitude, and saw-tooth structured glacial-interglacial

cycles (Chalk et al., 2017; Elderfield et al., 2012; McClymont et al., 2013; Rohling et al., 2014). The onset of MIS 11 coincided with the so-called "Mid-Brunhes Event", during which glacial-interglacial cycles underwent a further increase in amplitude due to the development of more prominent interglacial conditions than in the lukewarm interglacial periods that occurred earlier (Ao et al., 2020; Barth et al., 2018; Jouzel et al., 2007; Lüthi et al., 2008). T-V featured the largest amplitude changes in ice volume (sea level) of the past millions of years (e.g., Droxler et al., 2003)). The volume of the continental ice sheets during MIS 12 plausibly exceeded that of the last glacial maximum (Rohling et al., 1998), while extensive polar ice melting during MIS 11 (Blackburn et al., 2020) caused sea level to rise up to several meters above present levels (Raymo and Mitrovica, 2012; Dutton et al., 2015). These lines of evidence pose a serious challenge to the theory that ascribes Quaternary glaciations to orbital forcing (Milanković, 1941) and point to the potentially important role of climate feedbacks (Berger and Wefer, 2003) to explain the occurrence of the highest amplitude glacial termination at a time of comparatively small orbital forcing (e.g., Imbrie and Imbrie, 1980; Paillard, 2001). Changes in atmospheric CO_2 concentrations and continental ice volume (sea level) have been proposed as important climate feedbacks to explain the climate changes associated with the Middle to Late Pleistocene glacial-interglacial cycles (Chalk et al., 2017), given their impact on the radiative forcing of climate on 10^2-10^4-year timescales (Hansen et al., 2007, 2013; Rohling et al., 2018). Recent studies have provided detailed documentation of the atmospheric CO_2 changes around T-V (Nehrbass-Ahles et al., 2020), while the timing of the variations in global ice volume (sea level) and their relationships with orbital forcing around this key glacial-interglacial transition remain less well documented.

Discerning the different role played by orbital forcing and climate feedbacks and solving the above-mentioned open issues calls for precisely and independently (i.e., radioisotopically) dated records that can be compared with the insolation time-series that rely on the so-called "orbital solutions" (Laskar et al., 2004). A reliable chronological framework is available for the last glacial-interglacial cycle (e.g., Lambeck et al., 2014; Dutton and Lambeck, 2012), while the chronology of older ice-volume (sea-level) changes is generally based on the alignments of relative sea level (RSL) records to other well-dated paleoclimate time series (Rohling et al., 2009; Grant et al., 2014), and thus lack direct age control. This also affects our ability to decipher the so-called meltwater pulse events, relatively brief periods of rapid sea-level rise (e.g., Fairbanks et al., 1989; Deschamps et al., 2012) and meltwater release to the polar oceans that impact ocean circulation and climate on regional to global scales (Denton et al., 2010; Marino et al., 2015; Rohling et al., 2019; Weber et al., 2014).

The so-called "aggradational successions" of the Paleo Tiber River, central Italy, represent a radioisotopically dated (^{14}C and $^{40}Ar/^{39}A$) system of morpho-sedimentary units that formed in response to sea-level rise during the last eight glacial-interglacial transitions (Karner and Renne, 1998; Karner and Marra, 1998; Florindo et al., 2007; Marra et al., 2008, 2013, 2016a, 2016b; Marra and Florindo, 2014; Luberti et al., 2017). This composite record can thus provide key radioisotopic chronological constraints that generally lack in the Middle Pleistocene sea-level records, and that thus can be used to better evaluate the relationship between insolation changes and sea-level oscillations. We focus on the sedimentological features and geochronological constrains of new investigated sections of the San Paolo Formation (SPF, Fig. 1), belonging to the system of aggradational successions of the Paleo Tiber River, to refine the $^{40}Ar/^{39}Ar$ chronology of the glacial-interglacial sea-level change between ~450 ka and ~400 ka. Specifically, we integrate recently reported $^{40}Ar/^{39}Ar$ age determinations of the late stages of MIS 11c (Pereira et al., 2020) with new $^{40}Ar/^{39}Ar$ dating and tephrochronological constraints through the late stages of the MIS 12. This dataset allows refining in unprecedented detail the timing of rapid (or even abrupt) ice-sheet melting during late MIS 12 and around T-V, i.e., the glacial-interglacial transition featuring the highest amplitude of change over the last millions of years (e.g., Droxler et al., 2003).

2. Background information and geological setting

2.1. Tectonic and volcanological setting of the tyrrhenian margin

The Tyrrhenian Sea margin of central Italy, where the Tiber River and its valleys are located, developed as a back-arc basin since the Miocene (Malinverno and Ryan, 1986; Patacca et al., 1990), while the Paleo-Tiber delta formed southwest of Rome around 800 ka (Marra and Florindo, 2014). This region was subsequently affected by intense, explosive volcanic activity that formed the so-called "Roman Magmatic Region", which was active during Middle to Late Pleistocene (Conticelli and Peccerillo, 1992). Two main uplift phases at ~800 ka and since ~250 ka have led to a progressive seaward migration of the coast (Marra et al., 2019a).

Throughout this period, the sedimentary processes in the coastal and in the inland area were mainly controlled by the interaction between tectonic vertical movements and glacio-eustatic fluctuations (Luberti et al., 2017). Based on the comparison between the average uplift rate of the last 250 ka (0.24 mm/yr, Marra et al., 2019a) and the sedimentation rate during the aggradational phases (e.g., 2.3 mm/yr), Marra et al. (2019b) concluded that glacio-eustasy overrides the tectonic effects, which only impact the accommodation space, and, in turn, the total thickness (rather than the timing of deposition) of each aggradational succession.

2.2. The aggradational sedimentary successions of the paleo Tiber River

The hydrographic network of the Paleo Tiber River developed over a broad area that extends ~100 km north and south of the modern delta since the Late Pliocene-Early Pleistocene, in response to both regional uplift and glacioeustatic oscillations (e.g., Mancini et al., 2007) (Fig. 2). The so-called "aggradational successions" that fill (ed) the valleys of the (Paleo) Tiber River have thicknesses of up to 70 m (Marra et al., 2008, 2013) and consist each of a basal unconformity surface upon which a fining-upward sequence of gravel, sand, silt, and clay deposited (Karner and Marra, 1998). Sedimentological and stratigraphic analyses of these successions, argon-argon ($^{40}Ar/^{39}Ar$) and radiocarbon (^{14}C) dating of the interspersed tephra and peat layers, and complementary paleomagnetic constraints collectively demonstrate the dominant control of the Pleistocene glacial-interglacial sea-level changes on their deposition (Karner and Renne, 1998; Karner and Marra, 1998; Florindo et al., 2007; Marra et al., 2008, 2013, 2016a, 2016b, 2013, 2016b; Marra and Florindo, 2014; Luberti et al., 2017). Specifically, shoreline retreat and sea-level lowering during glacial periods lead to the progressive incision of a basal erosional surface, while the fining-upward successions of clastic sediments that drape over these surfaces represent the sedimentary response of the Paleo Tiber River to sea-level rise at glacial terminations until highstand conditions are established (Fig. 2).

The intense explosive activity of the regional volcanic districts fed by potassium-rich magma (Conticelli and Peccerillo, 1992) ensures robust chronological constraints through high-precision $^{40}Ar/^{39}Ar$ dating of the numerous tephra layers that occur within the sedimentary successions of the Paleo Tiber River (Alvarez et al.,

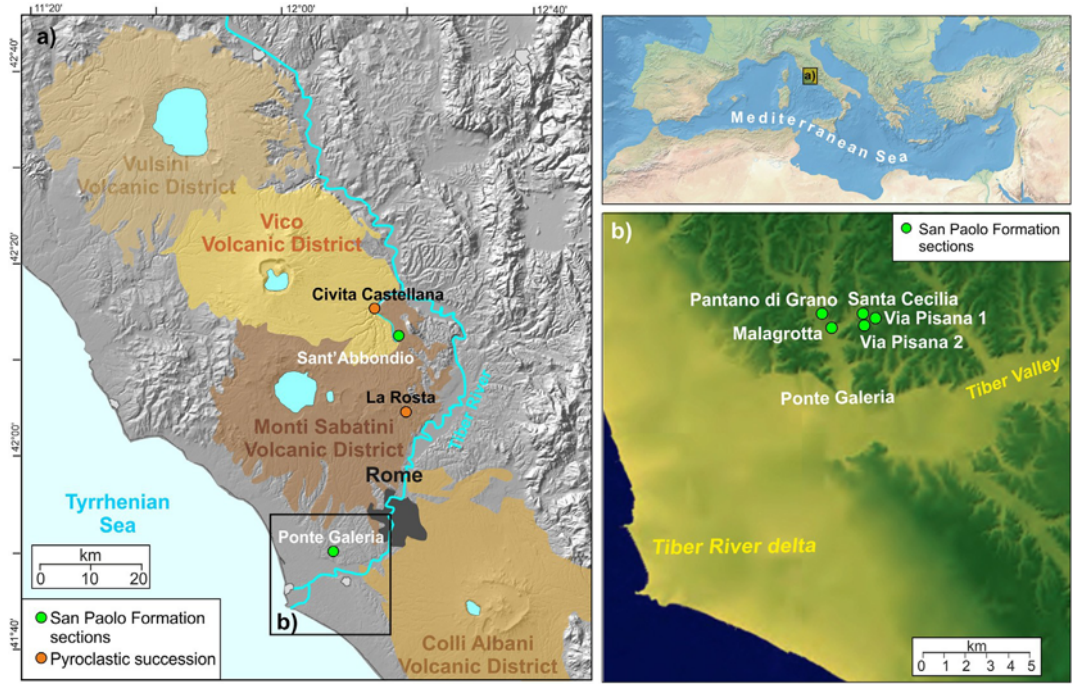

Fig. 1. Reference maps of the study area. a) Shaded relief, digital elevation model (DEM) image of the lower portion of the hydrographic network of the Tiber River, within the domain of the Latium volcanic districts, showing the locations of the investigated San Paolo Formation (Sant'Abbondio) and of the pyroclastic succession (La Rosta sections). The location of previously investigated San Paolo Formation and pyroclastic sections are also shown. b) Details of the Ponte Galeria area with the location of the individual sections belonging to the San Paolo Formation.

1996; Karner and Renne, 1998). Moreover, geochemical fingerprinting of the various eruptive events allows long-distance correlation among tephra deposits originated from the same eruption (e.g., Giaccio et al., 2019; Pereira et al., 2020).

The MIS 11 sections that are described in the present work are part of a complex morpho-stratigraphic setting, several km wide and up to 40 m in thickness, exposed by quarry excavations in the Tiber delta area. Such outcrops show that the sedimentary deposits belonging to the San Paolo Formation (Marra and Rosa, 1995; Karner and Marra, 1998) are constituted by a fining upward succession with a 4–6 m thick basal layer of coarse gravel (diameter of the pebbles ::;10 cm) filling the deepest portion of a set of incised valleys occurring at 25–30 m a.s.l., abruptly passing to a 20–30 m thick silty-clayey package of sediments with top at ~55 m a.s.l. Biostratigraphic, sedimentologic (Conato et al., 1980) and sequence stratigraphic (Milli, 1997, Milli et al., 2008) investigations have characterized these sediments as a vertical succession of fluvial (gravel and sand) to coastal and lagoon (silt and clay) deposits. Overall, these stratigraphic and sedimentological features occur as a ubiquitous, distinctive tract of the San Paolo Formation, as well as of other similar aggradational successions of the Paleo Tiber River delta, systematically observable over a wide area. They, thus, cannot be related to accidental, local change of the hydrological network, but to a phenomenon acting on a much wider spatial scale, able to drive large scale and near synchronous change of the depositional processes, such as the sea level change.

2.3. Stratigraphy and chronology of the San Paolo Formation (~450–400 ka)

The San Paolo Formation (SPF, Karner and Renne, 1998; Karner and Marra, 1998, 2003; Marra et al., 2016a) is a sedimentary succession (Fig. 3) of the Roman coastal area that is studied here to constrain the timing of the RSL fluctuations during the glacial MIS 12, termination V (T-V), and the highstand of the interglacial MIS 11. Geochemical and $^{40}Ar/^{39}Ar$ data acquired for the four primary and sub-primary tephra layers (SPF1 through SPF4) interbedded in the SPF sediments and in the proximal pyroclastic succession of the Vico Volcano allowed a robust tephrochronological correlation between SPF and Vico Volcano, resulting in a composite SPF section (Pereira et al., 2020), which reconciled some previous misinterpretations (Fig. 3). Specifically, Pereira et al. (2020) revised the altitude, the age, and the tephrostratigraphic attribution of the tephra layer SPF2 (sample R94-30C) of Malagrotta waste refusal site, which had previously been dated at 423.5 ± 5 ka, (2σ uncertainties; Karner and Renne, 1998). Pereira et al. (2020) demonstrated that the layer SPF2 (R94-30C) was located at higher altitude in the SPF succession and that it correlates with the first Plinian eruption of Vico Volcano (Vico a, 414.8 ± 2.2 ka, 2σ uncertainties), and that therefore matches SPF3 layer (Fig. 3). As consequence, the layer SPF2 was removed from the sketch of the SPF section that is reported in Fig. 3.

The other three tephra layers recognized in the SPF sections were labeled SPF1, SPF3a, and SPF4 and were tephrochronologically constrained as summarized in the following (Fig. 3). The lowermost volcanoclastic layer SPF1 was dated at 436.5 ± 6.0 ka (2σ uncertainties, Marra et al., 2016a), but remained uncorrelated because of the unavailability of samples and later inaccessibility of the outcrop. The layer SPF3a was instead successfully correlated, by means of direct $^{40}Ar/^{39}Ar$ dating (406.5 ± 2.5 ka, 2σ uncertainties) and geochemical fingerprinting, to the second Plinian eruptions of Vico volcano (Vico b, 406.5 ± 2.4 ka, 2σ uncertainties; Pereira et al., 2020). Finally, the complex SPF4 fallout deposit (403.5 ± 4.2 ka, 2σ uncertainties) was interpreted by Pereira et al. (2020) as a result of mixing of two co-eruptive units (Fig. 3) attributable to: (a) an unknown Vico Volcano eruption postdating Vico b; and (b) the activity of the Colli Albani Centogocce (following the Pozzolane Nere caldera-forming eruption, Marra et al., 2009).

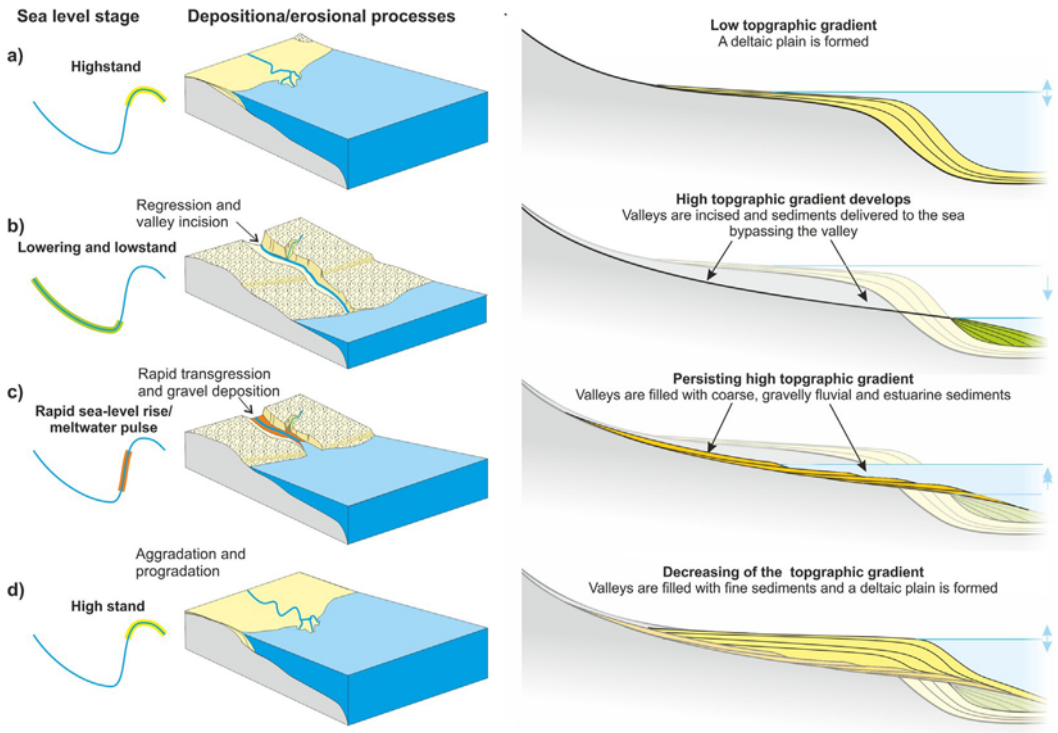

Fig. 2. Sketch explaining the mechanisms of formation of the Tiber River valley's aggradational succession in response to glacial-interglacial sea-level (continental ice-volume) change (cf. Karner and Renne, 1998; Karner and Marra, 1998; Florindo et al., 2007; Marra et al., 2008, 2013; 2016a, 2016b; Marra and Florindo, 2014; Luberti et al., 2017). An aggradational succession includes different facies, each diagnostic of specific sea-level conditions, tied to a specific stage of a "sawtooth" glacial-interglacial cycle (drawn on the left of each panel). The succession begins with the development of a deltaic plain (a) during an interglacial period, which features sea level standing at or up to a few meters above the present level for several millennia (highstand). Sea (base) level gradually lowers across the ensuing glacial period down to a lowstand at the glacial maximum (b), causing coastline regression, development of a basal erosional surface, valleys to be progressively incised, and sediments to be "bypassed" to the sea. During this phase, coarse gravel is transported along the river channel, but it is continuously removed and deposited offshore, in consequence of the progressive sea-level fall and deepening of the valley incision. The rapid sea-level rise (meltwater pulse) at the glacial termination (c) promotes rapid (abrupt) filling of the Tiber River valleys with a fining-upward sequence of clastic sediments that is characterised by a basal interval of distinct gravel deposition that abruptly switches to clay deposits. Gravel deposition marks the rapid to abrupt sea-level rise during the meltwater pulses, while the fine-grained sediments testify to the sea-level rise that leads to the (interglacial) highstad. Upon return to interglacial climate conditions (d), the sea-level highstand leads to another deltaic plain prior to another cycle. These sedimentary facies become exposed by continuous uplift affecting the Tiber River area that stem from eruptive phases of the regional volcanic districts (e.g., Karner et al., 2001a; Ferranti et al., 2006; Marra et al., 2016b). Blue arrows indicate whether sea level is lowering (downward arrow), rising (upward arrow), and standing (up-down arrow). (For interpretation of the references to colour in this figure legend, the reader is referred to the Web version of this article.)

3. Material and methods

3.1. The investigated sections

We present new $^{40}Ar/^{39}Ar$ age of a primary volcanic deposit (SAF0, Table 1) intercalated within a sedimentary succession cropping out at the Sant'Abbondio section, located ~35 km inland from the present-day coast, within a fluvial tributary valley of the Tiber River (Fig. 1), and of the SPF3/R94-30C layer from the coastal SPF sections of Ponte Galeria (Figs. 1 and 3). Moreover, we present wavelength dispersive spectroscopy (WDS) glass composition of four volcanic units occurring at Sant'Abbondio and at La Rosta sections (Table 1), providing two new tephrostratigraphic markers to the SPF aggradational succession. This dataset, combined with a review of all existing geochronological and geochemical data, allows a more firm constraint on the timing of the aggradational phases and sea-level change during the late stage of glacial MIS 12, T-V, and the highstand of interglacial MIS 11. Indeed, in spite of the inland location of the Sant'Abbondio section, Marra et al. (2019b) demonstrated how a large portion of the catchment basin of the paleo-fluvial system of the Tiber River was sensitive and responded synchronously to the sea-level fluctuations, as shown in the case of sections that are located even further inland than the Sant'Abbondio section.

Stratigraphic logs of the sections investigated in this study are reported in Fig. 4, while Table 1 summarizes the analysis performed in these sections.

3.2. $^{40}Ar/^{39}Ar$ dating

The $^{40}Ar/^{39}Ar$ dating of the Sant'Abbondio Unit Fall 0 (SAF0) and of layer SPF3 (R94-30C) were both performed at the Laboratoire des Sciences du Climat et de l'Environnement, Gif-sur-Yvette (France). Sample SAF0 was processed using the procedure from Pereira et al. (2020) and fully described in Nomade et al. (2010).

Sample R94-30C was prepared using the same procedure as in Nomade et al. (2011). Pristine sanidine crystals ranging in size between 500 μm and 300 μm were handpicked under a binocular microscope. The sample was irradiated for 120 min in the Cd-lined, in core CLICIT facility of the Oregon State University TRIGA reactor (IRR CO007). Interference corrections were based on the nucleogenic production ratios given in Balbas et al. (2016). After irradiation, the individual crystals were transferred into a copper 134 pits sample holder placed in a differential vacuum Teledyne Cetac window connected to the extraction line. Minerals were fused one by one using a 100Watts Teledyne Cetac CO_2 laser during 15 s with a 2.3 W power. Before fusion, each crystal underwent a 10 s

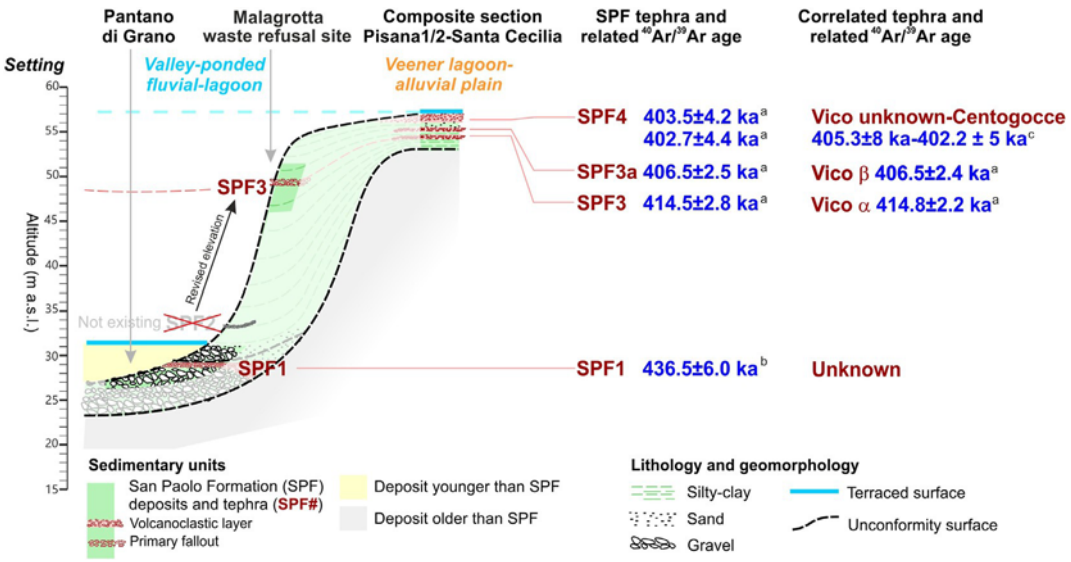

Fig. 3. Sedimentary, geomorphological, and tephrochronological framework of the aggradational succession of San Paolo Formation within the Roman coastal area of Ponte Galeria, spanning the MIS 12 through MIS 11 glacial-interglacial transition (modified from Pereira et al., 2020). The elevation and the age of what was previously referred as SPF2 layer, dated to 423.5 ± 5 ka (Karner and Renne, 1998, sample R94-30C), have been reappraised by Pereira et al. (2020), who demonstrated that it actually matches SPF3 layer, correlated to the Vico a eruption dated by these authors to 414.8 ± 2.2 ka. Data source; [a] Pereira et al. (2020); [b] Marra et al. (2016a); [c] Karner et al. (2001b); Gaeta et al. (2016). All the ages from the literature are here recalculated according to the same $^{40}Ar/^{39}Ar$ dating monitor standard for the Alder Creek sanidine standard ACs-2 at 1.1891 Ma (Niespolo et al., 2017).

Table 1
New and previous $^{40}Ar/^{39}Ar$, stratigraphic, and wavelength dispersive spectroscopy (WDS) analyses for each of the studied sections.

Geological setting	Site/Section	Unit ($^{40}Ar/^{39}Ar$ sample)	Investigations			Latitude and longitude
			Stratigraphy	$^{40}Ar/^{39}Ar$ age	WDS glass-composition	
Deltaic succession		SPF3 (R94-30C)	Pereira et al. (2020)	This study	Pereira et al. (2020)	41° 51′ 00″ N 12° 20′ 06″ E
Fluvial-pyroclastic succession	Sant'Abbondio	SAF1	This study	e	This study	42° 12′ 56.67″ N 12° 29′ 34.61″
		SAF0	This study	This study	This study	E
Monti Sabatini pyroclastic succession	La Rosta	LRF2	This study	Marra et al. (2020)	This study	42° 06′ 00.9″ N 12° 30′ 23.8″ E
		LRF1	This study	e	This study	

Extracted gases were purified by a SAES GP50 cold getter for 90s and then for 210 s by two hot SAES GP50 getters. The five Argon isotopes (i.e., ^{40}Ar, ^{39}Ar, ^{38}Ar, ^{37}Ar, and ^{36}Ar) were simultaneously analyzed using a NGX 600 mass spectrometer equipped with an array of 9 ATONA Faraday cups and an electron multiplier. Technical specifications and performances of the NGX 600 ATONA detector array are presented in Cox et al. (2020). Argon isotopes the following way: in the first run, ^{40}Ar, ^{39}Ar, and ^{38}Ar were measured simultaneously on 3 ATONA faraday cups, while the ^{36}Ar was measured using the electron multiplier. In a second time, after peak switching the ^{37}Ar was measured using the electron multiplier. Each isotope measurement corresponds to 15 cycles of 20-s integration time. Peak intensity data were reduced using ArArCALC V2.4 (Koppers, 2002). Neutron fluence J for each sample was calculated using co-irradiated Alder Creek sanidine standard ACs-2 at 1.1891 Ma (Niespolo et al., 2017) according to the K total decay constant of Renne et al. (2011). To determine the neutron flux of IRR CO007 flux monitors were placed in small pits framing the sample. Two standards from 3 pits around the unknown were measured to calculate R94-30C J-value (J ¼ 0.0005619 ± 0.00000045, 1s). Mass discrimination was monitored by analysis of 30 air pipettes of various beam sizes to verify the detectors linearity. These measurements are done automatically overnight before and after the unknown measurements (see supplementary material data table). Discrimination is calculated according to the $^{40}Ar/^{36}Ar$ ratio of 298.56 (Lee et al., 2006). Procedural blank measurements were achieved after every two or three unknowns depending of the beam sizes measured previously. For typical 5 min time blank backgrounds are between 1.7 10^{-4}V and 2.0 10^{-4}V for ^{40}Ar and 65 cps for ^{36}Ar (9.5 10^{-7} V equivalent).

New and previously published ages were calibrated against the K total decay constant of Renne et al. (2011) and the Alder Creek sanidine (ACs-2) optimization calculated standard age of 1.1891 Ma (Niespolo et al., 2017) was adopted. We retain the optimization calibration for the age of ACs-2 standard because it presents accurate and quantifiable uncertainties, and is independent of any astronomical tuning assumptions. Astronomical tuning has inherent uncertainties that are related, e.g., to the phase relationship between the proxy data and a specific "tuning target", such as the insolation curve or a specific orbital parameter (Laskar et al., 2004). This makes it difficult to quantify the overall chronological uncertainties associated with the tuned time series, thereby hindering a quantitative comparison with the chronologies based on $^{40}Ar/^{39}Ar$ dating (Renne et al., 2010). For consistency, all previously

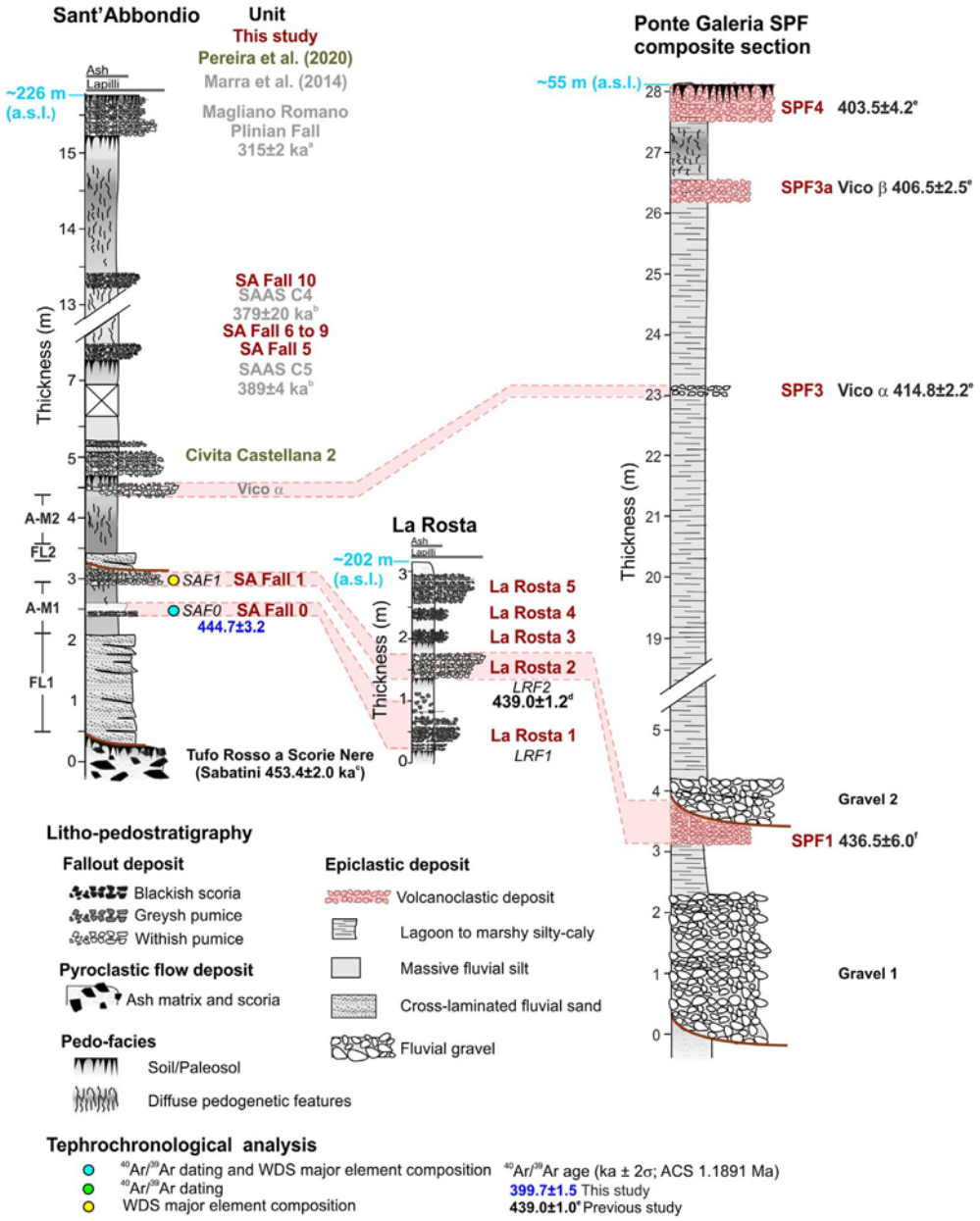

Fig. 4. Stratigraphic logs of the Sant'Abbondio and La Rosta Sections, investigated in this study. The sections are correlated with one another and with the San Paolo Formation (SPF), which is a composite section proposed by Pereira et al. (2020), located in the Roman (Ponte Galeria) coastal area (sections' locations are shown in Fig. 1). The stratigraphic positions of the samples used either for determining the geochemical composition of volcanic glass or analyzed for $^{40}Ar/^{39}Ar$ are also shown, while previously published $^{40}Ar/^{39}Ar$ ages are indicated as follows: (a) Sottili et al. (2010); (b) Marra et al. (2014); (c) Karner et al. (2001b); (d) Marra et al. (2020); (e) Pereira et al. (2020); (f) Marra et al. (2016a).

published $^{40}Ar/^{39}Ar$ ages are reported with their 2s analytical uncertainties including J and have been recalculated using the same ACs-2 flux standard age (i.e., 1.1891 Ma).

3.3. Major element analyses

Major and minor element compositions were determined on interstitial glass of pumices or scoria of the unit Sant'Abbondio Fall 0 and Fall 1 (SAF0 and SAF1) and La Rosta Fall 1 and Fall 2 (LRF1 and LRF2) (Table 1). Pumice and/or glass fragments were mounted on slides in epoxy resin, polished, and carbon coated. Electron microprobe analyser wavelength dispersive spectroscopy (EMPA-WDS) analyses were performed at the Istituto di Geologia Ambientale e Geoingegneria of the Italian National Research Council (IGAG-CNR, Rome). We used a CAMECA SX-50 EMPA, equipped with a five-wavelength dispersive spectrometer (WDS), and calibrated and set up with the same operating conditions as described in previous studies (e.g., (Giaccio et al., 2017). Analytical precision was evaluated by analyzing in the same run one external standard (Rhyolite RLS132 glasses from the United States Geological Survey). Results are shown in supplementary dataset 2 (SD 2). Geochemical analyses yielding analytical totals <93 wt% were rejected, whereas all analyses with higher totals were normalized to 100% on a volatile-free basis, that is, excluding Cl, SO_3, and F volatiles. Glass shards and micro-pumices were classified according to their geochemical composition using the Total Alkali vs Silica (TAS) classification diagram.

4. Results

4.1. Lithostratigraphy

4.1.1. Sant'Abbondio section - monti Sabatini Volcanic District

The Sant'Abbondio section consists of a ~15 m thick sedimentary succession of primary pyroclastic fall units (n ¼ 10), which are separated by fluvial deposits and/or paleosols that are tephrochronologically constrained between the Monti Sabatini Tufo Rosso a Scorie Nere eruption (TRSN, 453.4 ± 2.0 ka, recalculated in this study from Karner et al., 2001b) and Magliano Romano Plinian Fall (313.0 ± 2.0 ka; Sottili et al., 2010; Marra et al., 2014) (Figs. 3 and 4). Here we re-examined in detail the basal part of the Sant'Abbondio section that includes the pyroclastic layers SAF0 and SAF1 (Fig. 4).

The basal portion of the Sant'Abbondio section is a fluvial deposit mostly made of volcaniclastic sediments (FL1 in Figs. 4 and 5a), which overlie a deep paleosol that developed on the TRSN pyroclastic-flow (Figs. 4 and 5a). A 5e10 cm thick, dark grey, ash and lapilli fallout deposit (SAF0) with a discontinuous ash deposit at the bottom is: (i) intercalated with the fine-grained, upper part of the volcanoclastic deposit (AM-1a); and (ii) overlain by a ~50 cm thick, massive ash-mud deposit (AM-1b). Above the AM-1b sits a 20e30 cm thick, white pumice fallout (SAF1), on which deposited another ash-mud layer (AM-1c) that features incipient pedogenesis in the upper portion. Above AM-1c layer, a ~40 cm thick, sand-sized, planar bedded volcaniclastic deposit lays (FL-2), followed by a ~1 m thick, whitish ash-mud deposit (AM-2) capped by a well-developed paleosol (Fig. 5). A discontinuous pumice fallout layer is embedded at the base of this paleosol, which correlates with Vico a (Marra et al., 2014) that has an age of 414.8 ± 2.2 ka (Pereira et al., 2020). The interval above Vico a contains a pumice fall deposit, attributed to an unknown eruption of Sabatini (Civita Castellana 2; Pereira et al., 2020), and the so-called Sant'Abbondio Ash fall Succession (SAAS, 390 ± 4 ka, Marra et al., 2014) that is capped by the Magliano Plinian Plinian Fall (Fig. 4). The sedimentary interval comprised between the TRSN and Vico a at Sant'Abbondio deposited between ~453 ka and ~415 ka and is therefore coeval with the basal portion of the San Paolo Formation exposed in the Roman coastal area, i.e., the Pantano di Grano and Malagrotta Sections (Fig. 3).

4.1.2. La rosta section - monti Sabatini Volcanic District

The fallout succession exposed in La Rosta has been recently investigated by Marra et al. (2020). It consists of five pyroclastic units separated by incipient paleosols, overlain by the Magliano Romano Plinian fall (313.0 ± 2.0 ka, Sottili et al., 2010). The pumice fall La Rosta 2 (LRF2 in Fig. 4) was recently $^{40}Ar/^{39}Ar$ dated (439.0 ± 1.2 ka, recalculated in this study from Marra et al., 2020) and was potentially sourced in the central Sabatini Volcanic District (Marra et al., 2020).

The lowest unit (LR-1) of the La Rosta fall succession comprises a basal, 3 cm thick, dark grey ash-surge layer (LRS1), which is followed by a 12 cm thick lapilli fallout (LRF1) and by a 10 cm thick, ash-lapilli pyroclastic-flow deposit (LRP1) (Figs. 4 and 5b). A 30 cm thick, inversely graded, up to 3 cm in diameter holocrystalline lithic fallout layer (LRH1) closes the lower eruptive sequence at the top (Figs. 4 and 5b). Above a 40 cm-depth pedogenized ash layer, the eruptive unit (LRF2) consists of a ~35 cm-thick Plinian fallout made up of whitish, well vesicular, subaphyric pumice lapilli and includes a basal ~5 cm thick bed with abundant lava lithics. The Plinian unit LRF2 is overlain by three minor units composed by decimeter-thick ash layers and black, leucite-bearing (often analcimized) scoria lapilli fall deposits, rich in lava lithic inclusions and holocrystalline lithic clasts, the uppermost of which is ~60 cm thick (LRF3 to LRF5; Figs. 4 and 5b).

4.2. $^{40}Ar/^{39}Ar$ dating

Fifteen crystals of both sanidine and leucite from Sant'Abbondio Fall 0 (sample SAF0, Fig. 4, Table 1) were $^{40}Ar/^{39}Ar$ dated (supplementary dataset 1, SD 1). The relative probability diagram of this sample is multimodal (Fig. 6a) and reflects multiple crystal age populations. The youngest population contains seven crystals, allowing to calculate a weighted mean age of 444.7 ± 3.2 ka, MSWD ¼ 0.3 and P ¼ 0.9. The $^{40}Ar/^{36}Ar$ initial ratio given by the inverse isochron is of 299.6 ± 3.4 ka, equivalent to the atmospheric one of 298.56 ka (Lee et al., 2006), confirms the absence of argon excess or of argon fractioning in the sample.

The relative probability diagram of sample R94-30C is

Fig. 5. Pictures of the investigated Sant'Abbondio and La Rosta sections. a) General view (left picture) and details (right pictures) of the basal interval of the MIS 11 Sant'Abbondio section (42° 12′ 56.67″ N, 12° 29′ 34.61″ E; elevation: 226 m a.s.l.), including the SAF0 and SAF1, lying on the paleosol developed on the Tufo Rosso a Scorie Nere (TRSN). b) General view of the La Rosta section including the investigated LRF1 and LRF2 units (42° 06′00.9″N, 12° 30′23.8″E; elevation: 202 m a.s.l.).

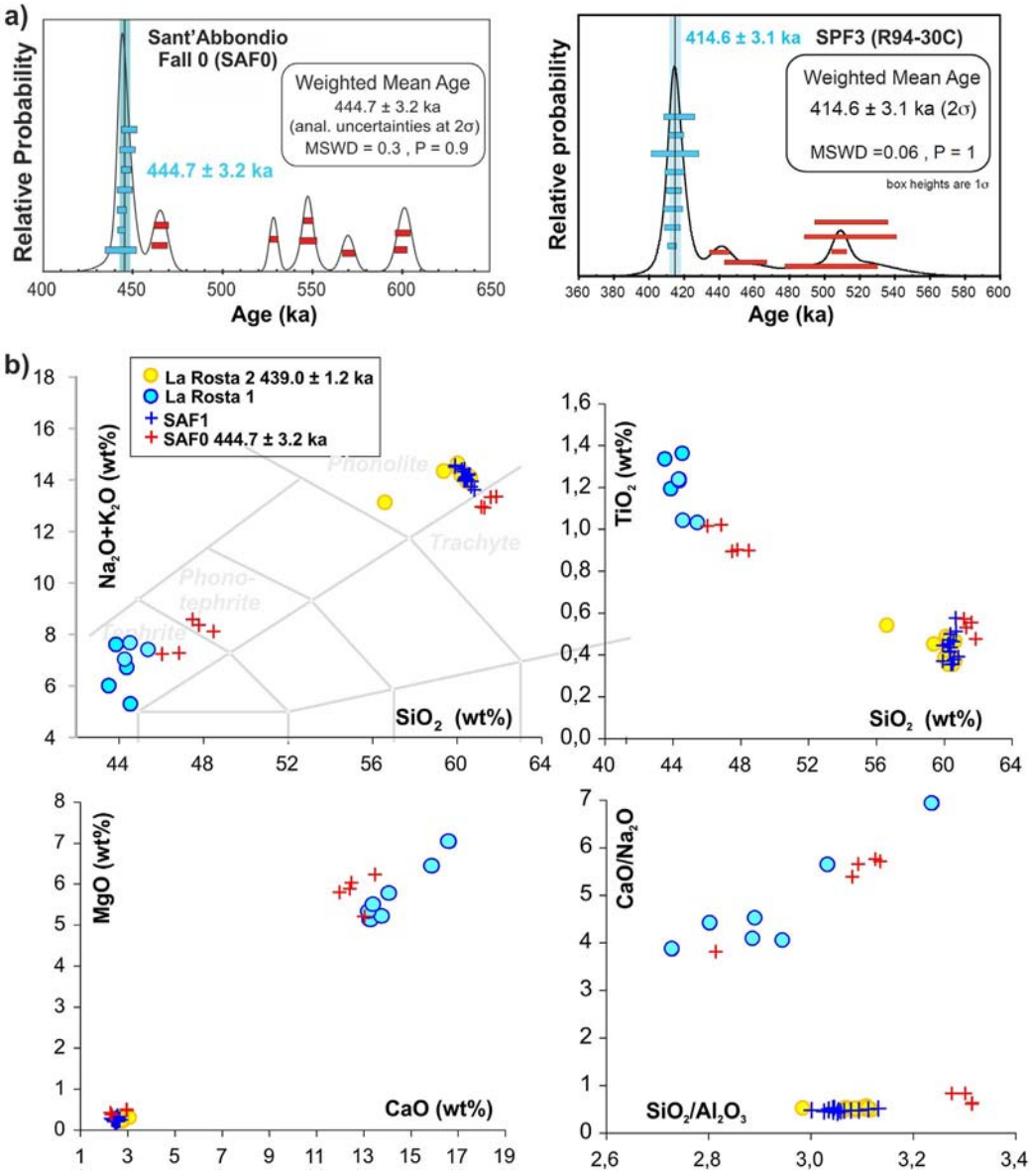

Fig. 6. Age and geochemistry of the investigated tephra layers. a) Single grain $^{40}Ar/^{39}Ar$ age of SAF0 and SPF3 (R94-30C) on single grain presented as probability diagram; b) total alkali versus silica diagram (Le Maitre, 2002) and representative bivariate diagrams for the tephra from the La Rosta (LRF1 and LRF2) and Sant'Abbondio (SAF0 and SAF1) sections.

multimodal like SAF0, indicating clearly several populations of contaminating xenocrysts, ranging between 440.7 ± 11.4 ka up to 521.8 ± 37.6 ka (Fig. 6a). The youngest population contains eight crystals, allowing to calculate a valid weighted mean age of 414.6 ± 3.1 ka (2s, MSWD ¼ 0.06 and P ¼ 1.0; Fig. 6a). The $^{40}Ar/^{36}Ar$ initial ratio given by the inverse isochron is 298.7 ± 3.0 ka, identical within uncertainties with the atmospheric reference of 298.56 (Lee et al., 2006), showing no excess argon in this population. The new age we present here for the layer SPF3 (R94-30C) at 414.6 ± 3.1 ka is consistent with that of Vico a (414.8 ± 2.2 ka; Pereira et al., 2020) and confirms the previous correlation based on geochemical composition (Pereira et al., 2020).

4.3. Geochemical composition of the tephra from Sant'Abbondio and La rosta sections

Full glass compositions are provided in supplementary dataset 2 (SD 2), while their classification according to the Total Alkali versus Silica (TAS) is shown in Fig. 6b.

Sant'Abbondio Fall 1 and Fall 2 e The composition of the glass from SAF0 is highly scattered, ranging from poorly differentiated tephritic and phono-tephrite terms, with MgO contents of up to 6 wt% (Fig. 6b) to an evolved trachyte composition with a silica content of ~61e62 wt% and ~13 wt% of alkali sum (Fig. 6b). The glass in SAF1 has instead an almost homogeneous phonolitic composition with SiO_2 contents of ~60e61 wt% and alkali sum of ~13.5e14.5 wt% (Fig. 6b).

La Rosta Fall 1 and 2 e The few analyzable glass shards found in the micolithic-rich juvenile clasts of LRF1 have a primitive tephrite composition, with a SiO_2 content of ~44 wt% (Fig. 6b) and a MgO contents as high as 7 wt% (Fig. 6b), similar to the primitive component of SAF1. The LRF2 pumice fall is instead characterized by a homogeneous phonolitic composition with SiO_2 content of ~60e61 wt% and alkali sum of ~13.5e14.5 wt%, similar to SAF1 (Fig. 6b).

5. Discussion

5.1. Correlation of inland and costal sections of the San Paolo Formation

The two pairs of pyroclastic units of the Sant'Abbondio and La Rosta sections investigated here (i.e., SAF0-SAF1 and LRF1-LRF2, Figs. 3 and 4) share similar stratigraphic and textural-lithological features, and geochemical composition. New and/or revised $^{40}Ar/^{39}Ar$ dating of these units brackets the interval between 444.7 ± 3.2 ka and 439 ± 1.2 ka. Specifically, the tephritic and phono-tephritic components of the heterogeneous SAF0 share a high degree of similarity with the La Rosta Fall 1 (i.e., LRF1), while the homogenous phonolitic glass composition of the white pumices from SAF1 precisely matches that of the La Rosta Fall 2 (i.e., LRF2, Fig. 6b and c). Therefore, stratigraphic order, lithology, and geochemical composition collectively suggest that the units from Sant'Abbondio and La Rosta sections can be confidently correlated with one another. This correlation also provides a refined and more precise geochronological constraint for the deposition of the SPF1 pumice layer of the basal part of Pantano di Grano section in Ponte Galeria for which the outcrop is no longer accessible but was previously dated at 436.5 ± 6.0 ka (Marra et al., 2016a). The age of the SPF1 collected at Pantano di Grano is statistically indistinguishable from that of LRF2 439.0 ± 1.2 ka. Also in terms of textural and lithological features, SPF1 is consistent with LRF2, as in the original field notes collected by one of us (F.M.) it is described as "a cross-bedded volcanic sand, prevalently made of mm-sized white pumice and loose pyroxene crystals", similar to LRF2. Therefore, by transferring the age of 439.0 ± 1.2 ka from La Rosta Fall 2 to SPF1 (Figs. 4 and 7) we (i) overcome the problems associated with inaccessibility of the outcrop and the associated lack of samples for $^{40}Ar/^{39}Ar$ dating and geochemical fingerprinting and (ii) substantially improve the precision of the dating of this SPF tephra.

5.2. Paleo Tiber River aggradational successions as a proxy for sea-level rise and significance of the basal coarse-grained sediments

The aggradational successions of the Paleo Tiber River consist each of a fining upward sequence (gravel, sand, silt, and clay) that deposit upon an unconformity surface (Karner and Marra, 1998). Following the conceptual model developed by Marra et al. (2008, 2016a), these successions provide a stratigraphic record (i.e., a full transgression cycle) of past glacial-interglacial sea-level cycles, while the "switch" from the coarse-grained (gravel) intervals at the base of these successions to the fine-grained (silt and clay) intervals at the top are diagnostic of rapid (abrupt) sea-level rise (meltwater pulses) at glacial terminations (Fig. 2).

In all the analyzed cases we deal with a chrono-morpho-stratigraphic context including:

i an unconformable boundary between a pre-aggradational geologic substrate and an overlying fining-upwards (aggradational) fluvial succession;
ii tight geochronologic constraints evidencing that the unconformable boundary corresponds to an erosional phase coeval with a sea-level lowstand;
iii a dm-to m-thick coarse sedimentary deposit (generally ascribable to well graded clean gravel and sand: GWSW, according to the Unified Soil Classification System) directly above the erosional surface, abruptly transitioning vertically over a few centimeters (jumping several divisions of sediment classified in the Unified Soil Classification System) to a several m-thick, fine-grained sedimentary package (i.e., high plasticity silt and clay with organic clay: CHOMH) (Marra et al., 2013).

Several lines of evidence support this interpretative model and, in turn, the reconstructions of the timing of ice-sheet melting during the late stages of glacial MIS 12 and at T-V based on the analysis of SPF aggradational successions presented in this study. First, conditions for the accumulation of the coarse gravel deposit only (co)existed at the onset of glacial terminations due to the: (i) low sea level at glacial maxima (e.g., Lambeck et al., 2014; Rohling et al., 2017), which steepens the gradients and, in turn, enhances the river competence (Fig. 2b and c); (ii) rapid melting of Apennine glaciers (Giraudi and Frezzotti, 1997) that releases large amount of clastic material, thereby increasing the sediment supply to the Tiber drainage basin; and (iii) overall increase in regional precipitation (Wagner et al., 2019). Second, the abruptness of the "sedimentary switch" that marks the transition from the gravel bed (up to ~10 m in thickness), through a thin (1–2 m in thickness) sand bed, into the thick (>30 m in thickness) silt and clay section claims for the sudden establishment of a low gradient, consistent with fast sea-level rise (meltwater pulse) and subsequent development of a sea-level highstand (Fig. 2d), in line with the observations across glacial termination I (Marra et al., 2008, 2013, 2016a). Third, there is an excellent agreement between the timing of meltwater pulses inferred from the Paleo Tiber River aggradational successions (Marra et al., 2008, 2016a), the rates of sea-level rise obtained from continuous, radiometrically constrained sea-level records (Grant et al., 2014), and the glacial termination ages in deep-ocean benthic foraminiferal $\delta^{18}O$ (Lisiecki and Raymo, 2005). This temporal consistency is particularly strong and convincing for the most recent Late Glacial-Holocene transition, which is constrained by ^{14}C dating and provides a proof of concept for the sedimentary model of Marra et al. (2008, 2016a). These studies highlight the agreement within uncertainties of the timing of deposition for the basal gravel of the most recent Tiber delta aggradational succession (between 15.0 ± 0.1 ka and 12.8 ± 0.1 ka) with the Bølling warming and MWP 1a (Deschamps et al., 2012; Brendryen et al., 2020). While abrupt stratigraphic changes may have purely climatic forcing (e.g., Blum et al., 1994), the coupled effect of climate and sea-level change in this case is straightforward as evidenced by coincidence with the meltwater pulse (see Fig. 1c in Marra et al., 2016a).

Fourth, Early versus Middle to Late Pleistocene successions exhibit markedly differently thicknesses of the respective clay sections (Karner et al., 2001a; Marra et al., 2008, 2013, 2016a). The increasing thickness of the clay sections through Early-Middle Pleistocene represents the plausible sedimentary response of the Paleo Tiber River to the higher amplitude, rapid terminations of the "sawtooth cycles" occurring after the Middle Pleistocene Transition and the Mid-Brunhes event (Jansen et al., 1986; Clark et al., 2009; Elderfield et al., 2012; Barth et al., 2018; Ao et al., 2020).

Finally, a tectonic origin (i.e., fault displacement) of these successions could be excluded, given that the gravel horizons systematically occur at the base of the aggradational sections and rest above an unconformable surface, which marks the intervening erosional phase during the sea-level lowstand at glacial maxima. Moreover, in a region as far as 100 km from the Apennines carbonate mountains, representing the source area for the coarse gravel sediment, fault displacement would cause an abrupt increase of accommodation space, along with a sudden drop in river transport capacity. Such elements rather cause the deposition of fine-grained, clayey deposits, as shown for the case of the Paleo-Tiber graben (Marra and Florindo, 2014).

5.3. Chronology of rapid ice-sheet melting prior to and during T-V, and relationship with insolation

In the coastal setting of the Ponte Galeria area, the volcanoclastic SPF1 deposit (equivalent to LRF2 in La Rosta section, see

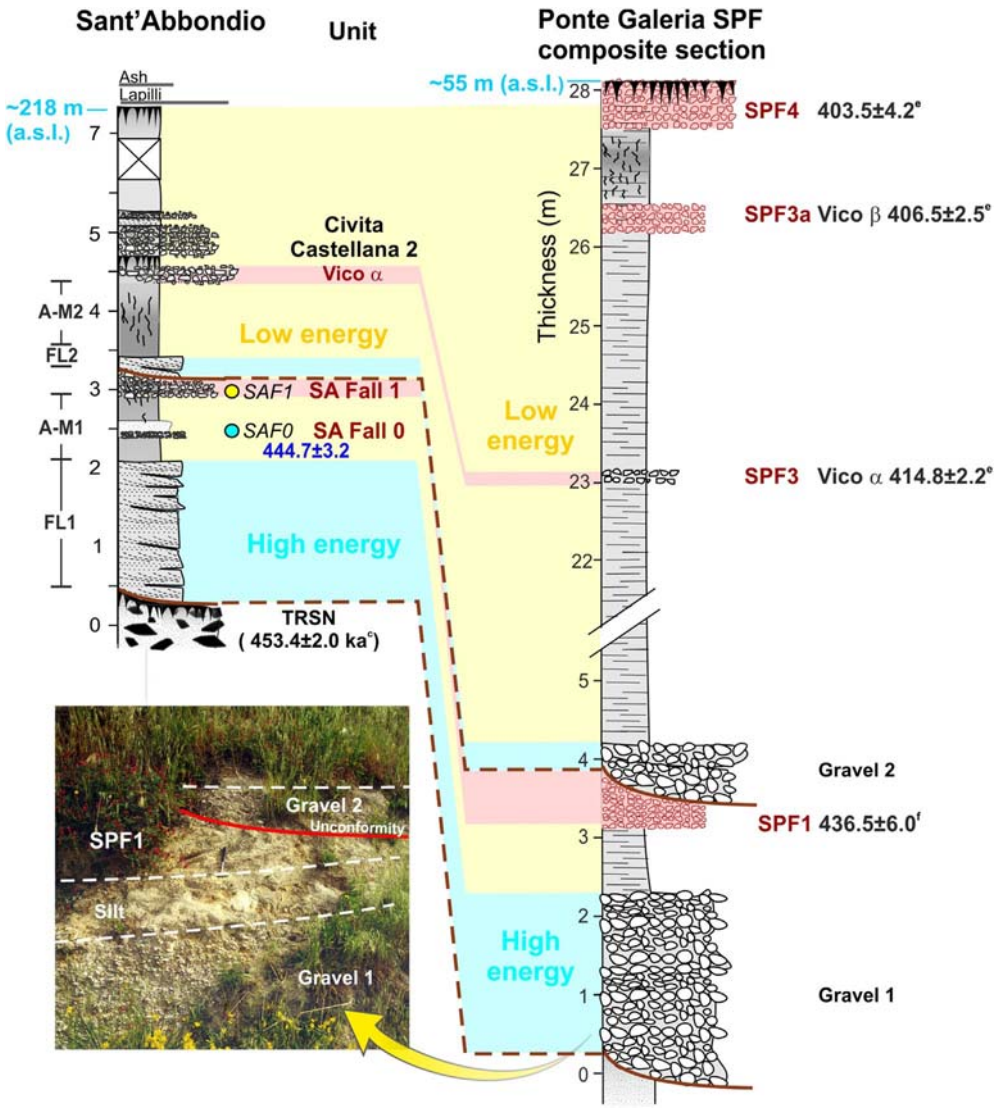

Fig. 7. Stratigraphic and tephrochronological correlations between the Sant'Abbondio section and San Paolo Formation (SPF) composite section in the Roman, Ponte Galeria, coastal areas. The blue and yellow bands indicated the high-energy and low-energy lithofacies, respectively. A picture of the basal portion of the SPF, outcropping at Pantano di Grano, is also shown. Litho-pedo-morphostratigraphic symbols as in Fig. 4. (For interpretation of the references to colour in this figure legend, the reader is referred to the Web version of this article.)

above) is found in between a fine-grained horizon and an erosion surface (unconformity) that separates two distinct gravel layers (Gravel 1 [G1] and 2 [G2], Fig. 4), thereby indicating a maximum age of 439.0 ± 1.2 ka for the unconformity that underlies G2 (Fig. 7). Similarly, in the Sant'Abbondio section the pyroclastic level SAF1, equivalent to the SPF1, is sandwiched in between two cross-laminated coarse sand beds (FL-1 and FL-2, Figs. 3, 5a and 7) that are separated by a fine-grained level (A-M1 in Figs. 3, 5a and 7) and an unconformity (Fig. 7). A low-energy sedimentary environment is then re-established above FL-2 and capped with the Vico a pumice fall, indicating that deposition of the upper aggradational succession of SPF ended at 414 ± 8 ka.

In summary, based on the similarity between the sequence of depositional and pedogenic-erosional events, constrained by the La Rosta 2 Fall and Vico a tephra layers, we can reasonably assume that the alternation of coarse- and fine-grained sediments observed at the Sant'Abbondio sections are the inland, fluvial counterpart of the high- and low-energy lithofacies of the SPF deposits found in the coastal setting of the Ponte Galeria area (Fig. 7). Specifically, the sand layers FL1 and FL2 at Sant'Abbondio section testify to sediment deposition in a high-energy setting and are interpreted here as the inland counterpart of (hence contemporaneous to) the coastal gravel levels G1 and G2 found in the coastal setting of Ponte Galeria (Fig. 7). In the following, we build on these findings to refine the chronology of the sea-level change during the last stages of MIS12 and MIS11, using the aggradational successions of Sant'Abbondio section.

The occurrence of the Sabatini TRSN eruption products dated at 453.4 ± 2.0 ka (recalculated in this study from Karner and Renne, 1998) at the very bottom of the Sant'Abbondio section adds an additional chronological constraint (i.e., a maximum age) to the onset of deposition of the basal gravel level G1 and its equivalent coarse sand layer FL1 at Sant'Abbondio that is capped by SAF0 (444.7 ± 3.2 ka). Considering the partial erosion and pedogenesis of the TRSN, we argue that G1 deposition plausibly occurred between ~450 ka and ~445 ka, which we take as the timing of a meltwater pulse event (i.e., MWP1, Fig. 8a). MWP1 coincides with the positive rates of sea-level change in the continuous, radiometrically

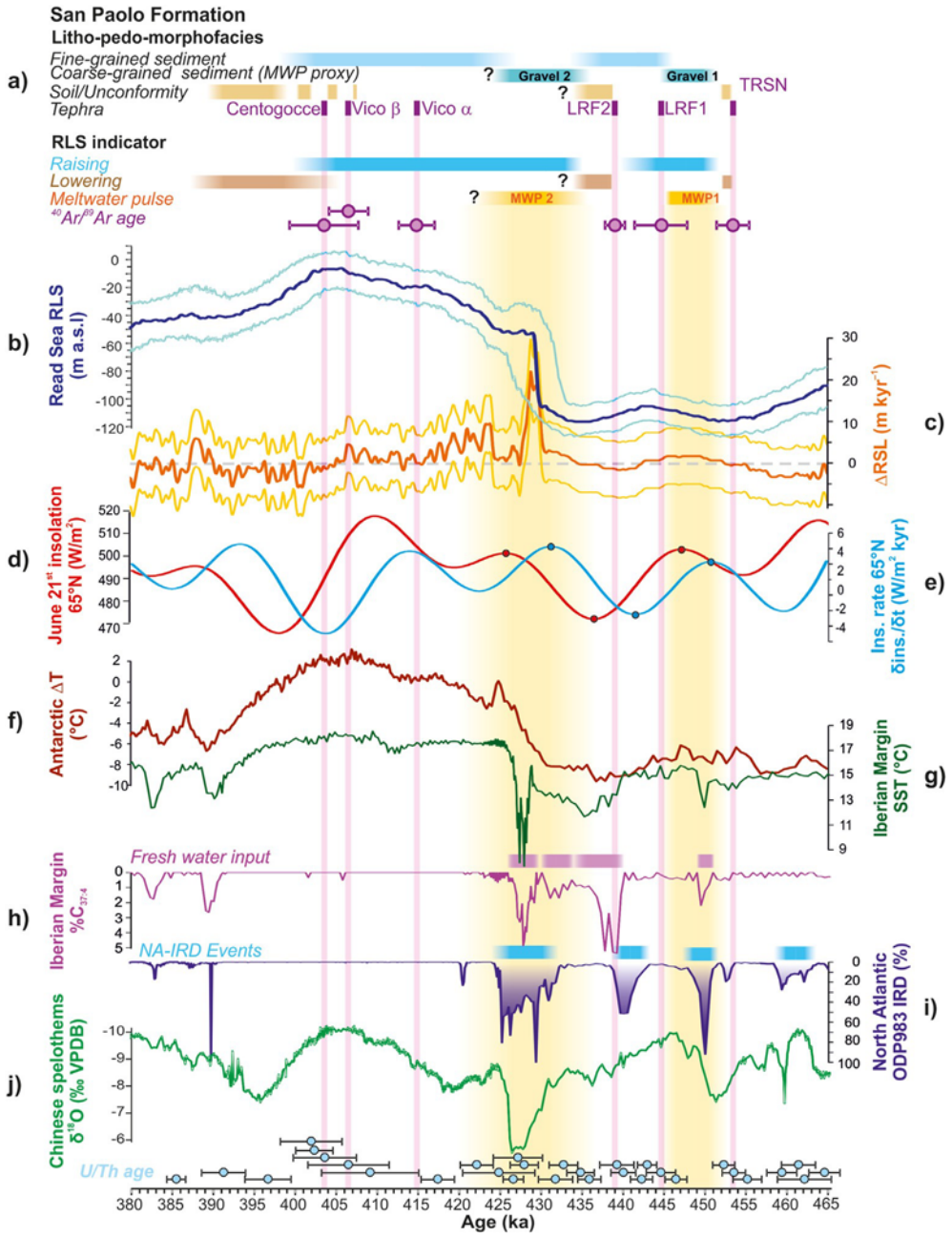

Fig. 8. Evidence of insolation, sea-level, and climate changes during the MIS 12 to MIS 11 transition. a) Main litho-pedo-stratigraphic and morphological features with related Relative Sea Level (RSL) indicators and $^{40}Ar/^{39}Ar$ geochronology of the San Paolo Formation aggradational succession. Note that tephra units are reported with their formal eruption names, regardless the dated sample labels. b) and c) relative seal level (RSL) change and rates of RSL change based on the "Red Sea method" (Grant et al., 2014). d) and e) June 21st insolation and insolation rates at 65° N (Laskar et al., 2004). f) Antarctic atmospheric temperature EPICA Dome C ice core (Jouzel et al., 2007). g) Iberian Margin Sea surface temperature (SST) variability at the Iberian Margin core MD03-2699 (Rodrigues et al., 2011). h) Percentage of tetraunsaturated ($C_{37:4}$) alkenones indicative of cold and potentially fresh surface waters at the Iberian Margin core MD03-2699 (Rodrigues et al., 2011). i) Ice-rafted debris (IRD) record from the North Atlantic Ocean Drilling Program (ODP) Site 983 (Barker et al., 2019). j) Chinese speleothem composite stable oxygen isotope ($\delta^{18}O$) time series. U/Th dating and associated 2σ uncertainties are also shown (Cheng et al., 2016). (For interpretation of the references to colour in this figure legend, the reader is referred to the Web version of this article.)

constrained sea-level record of Grant et al. (2014, Fig. 8b and c)) that is based on the "Red Sea method" (Siddall et al., 2003). This corroborates our finding and further highlights the sensitivity of the Paleo Tiber River aggradational successions to sea-level rise (Marra et al., 2008, 2016a, 2016a). In addition, MWP1 occurred under the deep glacial boundary conditions of MIS 12 and preceded by up to ~23 kyr the onset of T-V, for which the timing has also been radiometrically constrained using speleothem time series (Cheng et al., 2016).

The lower chronological limit of 439.0 ± 1.2 ka for the unconformity at the base of the upper gravel layer (G2) in the Ponte Galeria coastal area (see above) points to a multi-millennial scale return to more glaciated conditions (lowering sea level) that postponed deposition of SAF1 (equivalent to LRF2 and SPF1, Figs. 4 and 7) and promoted a drop in base level and attendant incision of the Paleo Tiber River valleys (Marra et al., 2008, 2016a, 2016a). This sea-level drop marked the descent into the "glacial maximum" of MIS 12 that preceded a second meltwater pulse event (MWP2) that

can be ascribed to T-V (Fig. 8). The La Rosta 2 (439.0 ± 1.2 ka) and Vico a (414.5 ± 2.8 ka) pumice fall horizons bracket the timing of MWP2 in our sections (Figs. 7 and 8). The upper and lower chronological limits of MWP2 cannot be further narrowed in the Paleo Tiber River aggradational successions, because: (a) a previously reported age constraint for the intermediate SPF2 layer (423.5 ± 5.1 ka, Marra et al., 2016a, Fig. 3) has been dismissed; and (b) the occurrence of LRF2 below the basal unconformity of G2 marks the timing of sea-level drop and provides no direct constraint to the timing of the meltwater pulse. However, we note that this age window (~439e415 ka) encompasses the T-V, marked by the maximum rate of sea-level rise reported by Grant et al. (2014) and centered at ~430 ka (Fig. 8). Therefore, in light of this broad chronological agreement and by analogy with other well constrained events of gravel deposition (e.g., Marra et al., 2016a), it is reasonable to assume that gravel level G2 deposited during the rapid (or even abrupt) sea-level rise (meltwater pulse) of T-V. Following T-V, continuous sedimentation in the SPF coastal plain sections at Ponte Galeria alludes to moderate sea-level rise until ~403 ka, when erosion or pedogenesis mark the onset of the sea level lowering and the beginning of the MIS 11 b substage, consistent with the Red Sea record (Grant et al., 2014, Fig. 8b).

The sequence of events at the MIS 12 to MIS 11 transition, characterized by two episodes of rapid ice-sheet melting during late MIS 12 and at T-V, separated by a brief interval of ice-volume growth, parallels relatively subtle changes (10 W m^{-2} to ~30 W m^{-2}) in summer insolation at the critical latitude of 65° N (Laskar et al., 2004, Fig. 8d). Specifically, ice-sheet melting and growth appear to coincide with positive and negative peaks, respectively, in the (rates of) insolation (change), with higher rates at MWP2 (i.e., T-V) than at MWP1 (Fig. 8d and e). This observation agrees with the notion that higher rates of insolation change may contribute to force a complete transition from glacial to interglacial climate states (Cheng et al., 2009), while it also suggests a potential role of negative insolation rates on ice-sheet growth.

5.4. Paleoclimate implications

The coupling of (rates of) insolation changes and ice-volume variations that we report for the MIS 12 to MIS 11 transition lends supports to the astronomical theory that ascribes the Northern Hemisphere ice-sheet melting to variations in the orbital parameters that control the insolation at the top of the atmosphere (Milanković, 1941; Imbrie and Imbrie, 1980; Paillard, 2001). Other studies have related the glacial-interglacial ice-volume (sea-level) changes to polar climate, and more specifically to changes in Antarctic air temperatures on both glacial-interglacial and millennial timescales (e.g., Shackleton et al., 2000; Siddall et al., 2003). This notion has provided the basis to "tune" the continuous sea-level reconstructions obtained from Red Sea sediment cores to Antarctic temperature records (Rohling et al., 2009). Subsequent construction of a radioisotopically constrained chronology for the same sea-level record has provided independent evidence for the close coupling of Antarctic temperatures and sea-level changes over the last ~500 kyr (Grant et al., 2014). An intermediate complexity model supported by paleoceanographic data through the last glacial cycle indicates that sea-level rise may arise from bipolar meltwater releases (Rohling et al., 2004). However, later studies concluded that insolation-forced Northern Hemisphere ice-sheet melting and Antarctic temperature rise may be explained by the so-called "bipolar seesaw" (Stocker and Johnsen, 2003), which, in turn, arises from the perturbation of the Atlantic Meridional Overturning Circulation linked meltwater release into the North Atlantic (Cheng et al., 2009; Barker et al., 2011). This causes asynchronous temperature and ice-sheet melting across the hemispheres (Marino et al., 2015; Rohling et al., 2019). The sequence of ice-volume (sea-level) changes documented here for the MIS 12 to MIS 11 transition fits this picture.

Meltwater pulses MWP1 (~450e445 ka) and MWP2 (~430 ka) occurred during periods of North Atlantic cooling and freshening (Fig. 8g and h) associated with the deposition of ice-rafted debris (IRD, Fig. 8i), equivalent to the so-called Heinrich events (Hemming, 2004), the weakening of the Asian Monsoon exemplified by positive shifts in the radioisotopically dated isotopic record of the Chinese speleothems (Fig. 8j), and the Antarctic warming (Fig. 8f). The occurrence of prominent IRD peaks associated with these meltwater pulses alludes to episodes of extensive iceberg calving in the North Atlantic, consistent with sustained melting of the circum-North Atlantic ice sheets (McManus et al., 1999) during both events. The occurrence of two, precisely dated tephra units bracketing the deposition of gravel level G1 in SPF allow a precise timing of the MWP1 (450e445 ka) reported here. However, we note that the rates of sea-level rise during MWP1 are quite modest (~1.6 m/kyr), compared with the maximum value of ~20 m/kyr observed at ~430 ka during MWP2 (Fig. 8c). The subdued rates of sea-level change in the record of Grant et al. (2014) during MWP1 may therefore be attributed to the lack of firm age constrains in this record that cause an apparent "relaxation" of the reconstructed rates of sea-level change. Note that this is plausible given that the chronology of the sea-level record of Grant et al. (2014) is better constrained at glacial terminations, where their approach (i.e., the synchronization of dust peaks in their sediment cores to the weak monsoon events of Cheng et al., 2009) exploits the large amplitude of the signals (higher signal to noise ratios). As for the deposition of the gravel level G2, although less precisely constrained by the available $^{40}Ar/^{39}Ar$ dating of the SPF succession, the coincidence with the high rates of sea-level change in the record of Grant et al. (2014) and with a distinct bipolar seesaw signature of the various paleoclimate records (Fig. 8) lends confidence to our interpretation that it reflects the rapid ice-sheet melting of T-V.

6. Concluding remarks

We refined the structure timing of the sea-level change at the transition between glacial MIS 12 and interglacial MIS11, by documenting an episode of ice-sheet melting in late MIS12 that preceded further continental ice growth prior to the extensive ice-volume decrease of T-V. Our study builds on new stratigraphic, geochemical, and geochronological analysis of two sections of the inland-coastal composite record of the San Paolo Formation "aggradational succession" of the Paleo Tiber River. The occurrence of two coarse-grained deposits at the base of these $^{40}Ar/^{39}Ar$ dated aggradational successions points to two distinct episodes of rapid sea-level rise e so-called meltwater pulses e that occurred at ~450e445 ka (MWP 1) and ~439e415 ka (MWP2), respectively. Comparison with radioisotopically constrained, continuous sea-level time series based on the so-called "Red Sea method" corroborates our findings and helps to further narrow the timing of MWP2 at ~430 ka. MWP2 coincided with T-V, the largest amplitude glacial termination of the last millions of years. On sub-orbital timescales, MWP 1 and MWP2 coincided with two bipolar seesaw events, expressed by Antarctic warming in response to North Atlantic Ocean freshening (due to meltwater release) and cooling. The timing of sea-level changes at the MIS 12 to MIS 11 transition appears closely coupled with that of Northern Hemisphere (rates of) summer insolation change, albeit the amplitude the insolation changes is relatively small (10 W m^{-2} to ~30 W m^{-2}). Feedback processes and/or high ice-sheet sensitivity to insolation (rates of) changes must therefore be considered to explain the ice-volume changes at the MIS 12 to MIS 11 transition.

Author's contribution

BG: Conceptualization, Validation, Investigation, Writing – original draft, Visualization, GM: Conceptualization, Validation, Writing – original draft, Visualization, FM: Conceptualization, Methodology, Validation, Investigation, Writing – original draft, Visualization, LM: Investigation, Validation, Data curation, Writing – review & editing, AP: Investigation, Methodology, Validation, Data curation, Writing – review & editing, GZ: Validation, Writing – review & editing, MG: Data curation, Validation, Writing – review & editing. NL: Data curation, Validation, Writing – review & editing. SN: Investigation, Methodology, Validation, Data curation, Writing – review & editing. DMP: Investigation, Validation, Writing – review & editing. GS: Investigation, Validation, Writing – review & editing. HG: Methodology, Validation, Data curation. VS: Methodology, Validation, Data curation

Declaration of competing interest

The authors declare that they have no known competing financial interests or personal relationships that could have appeared to influence the work reported in this paper.

Acknowledgments

We thank Cornel Olariu and an anonymous reviewer for providing insightful comments and suggestions that helped to improve clarity and quality of the paper. G.M. acknowledges support from the University of Vigo's programme to attract excellent research talent (RR04092017), a Beatriz Galindo Fellowship (2020), and a generous start-up package.

Appendix A. Supplementary data

Supplementary data to this article can be found online at https://doi.org/10.1016/j.quascirev.2021.106976.

References

Alvarez, W., Ammerman, A.J., Renne, P.R., Karner, D.B., Terrenato, N., Montanari, A., 1996. Quaternary fluvial-volcanic stratigraphy and geochronology of the Capitoline hill in Rome. Geology 24, 751–754.

Ao, H., Rohling, E.J., Stringer, C., Roberts, A.P., DekkersDupont-Nivet, G., Yu, J., Liu, Q., Zhang, P., Liu, Z., Ma, X., Zhou, W., Jin, Z., Xiao, G., Wang, H., Sun, Q., Yang, P., Peng, X., Shi, Z., Qiang, X., An, Z., 2020. Two-stage mid-Brunhes climate transition and mid-Pleistocene human diversification. Earth-Sci. Rev. 210, 103354.

Balbas, A., Koppers, A.A.P., Kent, D.V., Konrad, K., Clark, P.U., 2016. Identification of the short-lived Santa Rosa geomagnetic excursion in lavas on Floreana Island (Galapagos) by $^{40}Ar/^{39}Ar$ geochronology. Geology 44, 359–362, 10/f8kdpg.

Barker, S., Knorr, G., Conn, S., Lordsmith, S., Newman, D., Thornalley, D., 2019. Early interglacial legacy of deglacial climate instability. Paleoceanogr. Paleoclimatol. 34, 1455–1475.

Barker, S., Knorr, G., Edwards, L., Parrenin, F., Putnam, A.E., Skinner, L.C., Wolff, E., Ziegler, M., 2011. 800,000 years of abrupt climate variability. Science 334, 347–351.

Barth, A.M., Clark, P.U., Bill, N.S., He, F., Pisias, N.G., 2018. Climate evolution across the mid-Brunhes transition. Clim. Past 14, 2071–2087.

Berger, W.H., Wefer, G., 2003. On the dynamics of the ice ages: stage-11 paradox, mid-Brunhes climate shift, and 100-ky cycle. In: Droxler, A.W., Poore, R.S., Burckle, L.H. (Eds.), Earth's Climate and Orbital Eccentricity. The Marine Isotope Stage 11 Question. Geophysical Monograph 137, AGU, Washington, DC, pp. 41–60.

Blackburn, T., Edwards, G.H., Tulaczyk, S., Scudder, M., Piccione, G., Hallet, B., McLean, N., Zachos, J.C., Cheney, B., Babbe, J.T., 2020. Ice retreat in Wilkes basin of East Antarctica during a warm interglacial. Nature 583, 554–559.

Blum, M.D., Toomey, R.S., Valastro, S., 1994. Fluvial response to late quaternary climatic and environmental change, edwards plateau, Texas. Palaeogeogr. Palaeoclimatol. Palaeoecol. 108, 1–21.

Brendryen, J., Haflidason, H., Yokoyama, Y., Haaga, K.A., Hannisdal, B., 2020. Eurasian Ice Sheet collapse was a major source of Meltwater Pulse 1A 14,600 years ago. Nat. Geosci. 13, 363–368.

Chalk, T.B., Hain, M.P., Foster, G.L., Rohling, E.J., Sexton, P.F., Badger, M.P.S., Cherry, S.G., Hasenfratz, A.P., Haug, G.H., Jaccard, S.L., Martínez-García, A., PValike, H., Pancost, R.D., Wilson, P.A., 2017. Causes of ice age intensification across the Mid-Pleistocene Transition. Proc. Natl. Acad. Sci. Unit. States Am. 114, 13114–13119.

Cheng, H., Edwards, R.L., Broecker, W.S., Denton, G.H., Kong, X., Wang, Y., Zhang, R., Wang, X., 2009. Ice age terminations. Science 326, 248–252. https://doi.org/10.1126/science.1177840.

Cheng, H., Edwards, R.L., Sinha, A., Spötl, C., Yi, L., Chen, S., Lelly, M., Kathayat, G., Wang, X., Kong, X., Wang, Y., Ning, Y., Zhang, H., 2016. The Asian monsoon over the past 640,000 years and ice age terminations. Nature 534, 640–646.

Clark, P.U., Dyke, A.S., Shakun, J.D., Carlson, A.E., Clark, J., Wohlfarth, B., Mitrovica, J.X., Hostetler, S.W., McCabe, A.M., 2009. The last glacial maximum. Science 325, 710–714.

Conato, V., Esu, D., Malatesta, A., Zarlenga, F., 1980. New data on the Pleistocene of Rome. Quaternaria 22, 131–176.

Conticelli, S., Peccerillo, A., 1992. Petrology and geochemistry of potassic and ultrapotassic volcanism in Central Italy: petrogenesis and inferences on the evolution of the mantle sources. Lithos 28, 221–240.

Cox, S.E., Hemming, S.R., Tootell, D., 2020. The Isotopx NGX and ATONA Faraday amplifiers. Geochronology 2, 231–243. https://doi.org/10.5194/gchron-2-231-2020.

Denton, G.H., Anderson, R.F., Toggweiler, J.R., Edwards, R.L., Schaefer, J.M., Putnam, A.E., 2010. The last glacial termination. Science 328, 1652–1656.

Deschamps, P., Durand, N., Bard, E., Hamelin, B., Camoin, G., Thomas, A.L., Henderson, G.M., Okuno, J., Yokoyama, Y., 2012. Ice-sheet collapse and sea-level rise at the Bølling warming 14,600 years ago. Nature 483, 559–564.

Dutton, A., Lambeck, K., 2012. Ice volume and sea level during the last interglacial. Science 337, 216–219.

Droxler, A.W., Poore, R.Z., Burckle, L.H. (Eds.), 2003. Earth's Climate and Orbital Eccentricity – the Marine Isotope Stage Question. Geophys. Monogr. Ser., 137. American Geophysical Union, Washington, pp. 240–pp.

Dutton, A., Carlson, A.E., Long, A.J., Milne, G.A., Clark, P.U., DeConto, R., Horton, B.P., Rahmstorf, S., Raymo, M.E., 2015. Sea-level rise due to polar ice-sheet mass loss during past warm periods. Science 349, aaa4019.

Elderfield, H., Ferretti, P., Greaves, M., Crowhurst, S., McCave, I.N., Hodell, D., Piotrowski, A.M., 2012. Evolution of ocean temperature and ice volume through the mid-pleistocene climate transition. Science 337, 704–709.

Fairbanks, R.G., 1989. A 17,000-year glacio-eustatic sea level record: influence of glacial melting rates on the Younger Dryas event and deep-ocean circulation. Nature 342, 637–642.

Ferranti, L., Antonioli, F., Mauzc, B., Amorosi, A., Dai Pra, G., Mastronuzzi, G., Monaco, C., Orrù, P., Pappalardo, M., Radtke, U., Renda, P., Romano, P., Sansò, P., Verrubbi, V., 2006. Markers of the last interglacial sea-level high stand along the coast of Italy: tectonic implications. Quaternay International 145/146, 30–54.

Florindo, F., Karner, D.B., Marra, F., Renne, P.R., Roberts, A.P., Weaver, R., 2007. Radioisotopic age constraints for glacial terminations IX and VII from aggradational sections of the Tiber River delta in Rome, Italy. Earth Planet Sci. Lett. 256, 61–80. https://doi.org/10.1016/j.epsl.2007.01.014.

Gaeta, M., Freda, C., Marra, F., Arienzo, I., Gozzi, F., Jicha, B., Di Rocco, T., 2016. Paleozoic metasomatism at the origin of Mediterranean ultrapotassic magmas: constraints from time-dependent geochemistry of Colli Albani volcanic products (Central Italy). Lithos 244, 151–164.

Giaccio, B., Leicher, N., Mannella, G., Monaco, L., Regattieri, E., Wagner, B., Zanchetta, G., Gaeta, M., Marra, F., Nomade, S., Palladino, D.M., Pereira, A., Scheidt, S., Sottili, G., Wonik, T., Wulf, S., Zeeden, C., Ariztegui, D., Cavinato, G.P., Dean, J., Florindo, F., Leng, M., Macrì, P., Niespolo, E., Renne, P.R., Rolf, C., Sadori, L., Thomas, C., Tzedakis, C., 2019. Extending the tephra and palaeoenvironmental record of the Central Mediterranean back to 430 ka: a new core from Fucino Basin, central Italy. Quat. Sci. Rev. 225, 106003.

Giaccio, B., Niespolo, E.M., Pereira, A., Nomade, S., Renne, P.R., Albert, P.G., Arienzo, I., Regattieri, E., Wagner, B., Zanchetta, G., Gaeta, M., Galli, P., Mannella, G., Peronace, E., Sottili, G., Florindo, F., Leicher, N., Marra, F., Tomlinson, E.T., 2017. First integrated tephrochronological record for the last ~190 kyr from the Fucino Quaternary lacustrine succession, central Italy. Quat. Sci. Rev. 158, 211–234.

Giraudi, C., Frezzotti, M., 1997. Late Pleistocene glacial events in the central Apennines, Italy. Quat. Res. 48, 280–290.

Grant, K.M., Rohling, E.J., Ramsey, C.B., Cheng, H., Edwards, R.L., Florindo, F., Heslop, D., Marra, F., Roberts, A.P., Tamisiea, M.E., Williams, F., 2014. Sea-level variability over five glacial cycles. Nat. Commun. 5, 5076. https://doi.org/10.1038/ncomms6076.

Hansen, J., Sato, M., Kharecha, P., Russell, G., Lea, D.W., Siddall, M., 2007. Climate change and trace gases. Phil. Trans. R. Soc. Lond. A 365, 1925–1954.

Hansen, J., Sato, M., Russell, G., Kharecha, P., 2013. Climate sensitivity, sea level and atmospheric carbon dioxide. Phil. Trans. Math. Phys. Eng. Sci. 371, 20120294.

Hemming, S.R., 2004. Heinrich events: massive late Pleistocene detritus layers of the North Atlantic and their global climate imprint. Rev. Geophys. 42, RG1005 https://doi.org/10.1029/2003RG000128.

Imbrie, J., Imbrie, J.Z., 1980. Modeling the climatic response to orbital variations. Science 207, 943–953.

Jansen, J.H.F., Kuijpers, A., Troelstra, S.R.A., 1986. Mid-Brunhes climatic event: long-term changes in global atmosphere and ocean circulation. Science 232, 619–622.

Jouzel, J., Masson-Delmotte, V., Cattani, O., Dreyfus, G., Falourd, S., Hoffmann, G., Minster, B., Nouet, J., Barnola, J.M., Chappellaz, J., Fischer, H., Gallet, J.C.,

Johnsen, S., Leuenberger, M., Loulergue, L., Luethi, D., Oerter, H., Parrenin, F., Raisbeck, G., Raynaud, D., Schilt, A., Schwander, J., Selmo, E., Souchez, R., Spahni, R., Stauffer, B., Steffensen, J.P., Stenni, B., Stocker, T.F., Tison, J.L., Werner, M., Wolff, E.W., 2007. Orbital and millennial antarctic climate variability over the past 800,000 years. Science 317, 793e796.

Karner, D.B., Marra, F., 1998. Correlation of fluviodeltaic aggradational sections with glacial climate history: a revision of the Pleistocene stratigraphy of Rome. Geol. Soc. Am. Bull. 110, 748e758.

Karner, D.B., Marra, F., 2003. 40Ar/39Ar dating of Glacial Termination V and duration of the Stage 11 highstand. In: Droxler, A.W., Poore, R.Z., Burckle, L.H. (Eds.), Earth's Climate and Orbital Eccentricity: the Marine Isotope Stage 11 Question, vol. 137. American Geophysical Union, Geophysical Monograph, pp. 61e66.

Karner, D.B., Renne, P.R., 1998. 40Ar/39Ar geochronology of Roman volcanic province tephra in the Tiber River valley: age calibration of middle Pleistocene sea-level changes. Geol. Soc. Am. Bull. 110, 740e747.

Karner, D.B., Marra, F., Florindo, F., Boschi, E., 2001a. Pulsed uplift estimated from terrace elevations in the coast of Rome: evidence for a new phase of volcanic activity? Earth Planet Sci. Lett. 188, 135e148.

Karner, D.B., Marra, F., Renne, P.R., 2001b. The history of the Monti Sabatini and Alban Hills volcanoes: groundwork for assessing volcanic-tectonic hazards for Rome. J. Volcanol. Geoth. Res. 107, 185e219.

Koppers, A.A.P., 2002. ArArCALC e software for $^{40}Ar/^{39}Ar$ age calculations. Comput. Geosci. 28, 605e619.

Lambeck, K., Rouby, H., Purcell, A., Sun, Y., Sambridge, M., 2014. sea Level and global ice volumes from the last glacial maximum to the holocene. Proc. Natl. Acad. Sci. Unit. States Am. 111, 15296e15303.

Laskar, J., Robutel, P., Joutel, F., Gastineau, M., Correia, A.C.M., Levrard, B., 2004. A long-term numerical solution for the insolation quantities of the Earth. Astron. Astrophys. 428, 261e285.

Lee, J.Y., Marti, K., Severinghaus, J.P., Kawamura, K., Hee-Soo, Y., Lee, J.B., Kim, J.S., 2006. A redetermination of the isotopic abundances of atmospheric Ar. Geochimica et Cosmochimica. Acta 70, 4507e4512. https://doi.org/10.1016/j.gca.2006.06.1563.

Lisiecki, L.E., Raymo, M.E., 2005. A Pliocene-Pleistocene stack of 57 globally distributed benthic $\delta^{18}O$ records. Paleoceanography 20, PA1003.

Luberti, G.M., Marra, F., Florindo, F., 2017. A review of the stratigraphy of Rome (Italy) according to geochronologically and paleomagnetically constrained aggradational successions, glacio-eustatic forcing and volcano-tectonic processes. Quat. Int. 438, 40e67. https://doi.org/10.1016/j.quaint.2017.01.044.

Lüthi, D., Le Floch, M., Bereiter, B., Blunier, T., Barnola, J.-M., Siegenthaler, U., Raynaud, D., Jouzel, J., Fischer, H., Kawamura, K., Stocker, T.F., 2008. High-resolution carbon dioxide concentration record 650,000e800,000 years before present. Nature 453, 379e382.

Malinverno, A., Ryan, W.B.F., 1986. Extension in the Tyrrhenian sea and shortening in the Apennines as results of arc migration driven by sinking of the lithosphere. Tectonics 5, 227e245.

Mancini, M., D'Anastasio, E., Barbieri, M., De Martini, 2007. Geomorphological, paleontological and 87Sr/86Sr isotope analyses of early Pleistocene paleo shorelines to define the uplift of Central Apennines (Italy). Quat. Res. 67, 487e501. https://doi.org/10.1016/j.yqres.2007.01.005.

Marino, G., Rohling, E.J., Rodríguez-Sanz, L., Grant, K.M., Heslop, D., Roberts, A.P., Stanford, J.D., Yu, J., 2015. Bipolar seesaw control on last interglacial sea level. Nature 522, 197e201.

Marra, F., Florindo, F., 2014. The subsurface geology of Rome: sedimentary processes, sea-level changes and astronomical forcing. Earth Sci. Rev. 136, 1e20.

Marra, F., Rosa, C., 1995. Stratigrafia e assetto geologico dell'area romana. In: Funiciello, R. (Ed.), La Geologia di Roma". Mem. Des. d, vol. 50. Carta Geol. d'It, pp. 49e118.

Marra, F., Florindo, F., Boschi, E., 2008. History of glacial terminations from the Tiber River, Rome: insights into glacial forcing mechanisms. Paleoceanography 23, 1e17. https://doi.org/10.1029/2007PA001543.

Marra, F., Karner, D.B., Freda, C., Gaeta, M., Renne, P.R., 2009. Large mafic eruptions at the Alban Hills Volcanic District (Central Italy): chronostratigraphy, petrography and eruptive behavior. J. Volcanol. Geoth. Res. 179, 217e232. https://doi.org/10.1016/j.jvolgeores.2008.11.009.

Marra, F., Sottili, G., Gaeta, M., Giaccio, B., Jicha, B., Masotta, M., Palladino, D.M., Deocampo, D., 2014. Major explosive activity in the Sabatini Volcanic District (central Italy) over the 800-390 ka interval: geochronological - geochemical overview and tephrostratigraphic implications. Quat. Sci. Rev. 94, 74e101. https://doi.org/10.1016/j.quascirev.2014.04.010.

Marra, F., Rohling, E.J., Florindo, F., Jicha, B., Nomade, S., Pereira, A., Renne, P.R., 2016a. Independent 40Ar/39Ar and 14C age constraints on the last five glacial terminations from the aggradational successions of the Tiber River, Rome (Italy). Earth Planet Sci. Lett. 449, 105e117. https://doi.org/10.1016/j.epsl.2016.05.037.

Marra, F., Florindo, F., Anzidei, M., Sepe, V., 2016b. Paleo-surfaces of glacio-eustatically forced aggradational successions in the coastal area of Rome: assessing interplay between tectonics and sea-level during the last ten interglacials. Quat. Sci. Rev. 148, 85e100. https://doi.org/10.1016/j.quascirev.2016.07.003.

Marra, F., Gaeta, M., Jicha, B.R., Nicosia, C., Tolomei, C., Ceruleo, P., Florindo, F., Gatta, M., La Rosa, M., Rolfo, M.F., 2019a. MIS 9 to MIS 5 terraces along the Tyrrhenian Sea coast of Latium (central Italy): assessing interplay between sea-level oscillations and tectonic movements. Geomorphology 346, 106843. https://doi.org/10.1016/j.geomorph.2019.106843.

Marra, F., Costantini, L., Di Buduo, G.M., Florindo, F., Jicha, B.R., Monaco, L., Palladino, D.M., Sottili, G., 2019b. Combined glacio-eustatic forcing and volcano-tectonic uplift: geomorphological and geochronological constraints on the Tiber River terraces in the eastern Vulsini Volcanic District (central Italy). Global Planet. Change 182, 103009. https://doi.org/10.1016/j.gloplacha.2019.103009.

Marra, F., Bozzano, F., Cinti, F.R., 2013. Chronostratigraphic and lithologic features of the Tiber River sediments (Rome, Italy): Implications on the post-glacial sea-level rise and Holocene climate. Glob. Planet. Change 107, 157e176. https://doi.org/10.1016/j.gloplacha.2013.05.002.

Marra, F., Castellano, C., Cucci, L., Florindo, F., Gaeta, M., Jicha, B., Palladino, D.M., Sottili, G., Tertulliani, A., Tolomei, C., 2020. Monti Sabatini and Colli Albani: the dormant twin volcanoes at the gates of Rome. Sci. Rep. 10 (1), 8666.

McClymont, E.L., Sosdian, S.M., Rosell-Mel e, A., Rosenthal, Y., 2013. Pleistocene sea-surface temperature evolution: early cooling, delayed glacial intensification, and implications for the mid-Pleistocene climate transition. Earth-Sci. Rev. 123, 173e193.

McManus, J.F., Oppo, D.W., Cullen, J.L., 1999. A 0.5-million-year record of millennial-scale climate variability in the North Atlantic. Science 283, 971e975.

Milankovitch, M.R., 1941. Serb, vol. 132. Acad. Special Publ., Belgrade.

Milli, S., 1997. Depositional setting and high-frequency sequence stratigraphy of the middle-upper Pleistocene to holocene deposits of the roman basin. Geol. Rom. 33, 99e136.

Milli, S., Moscatelli, M., Palombo, M.R., Parlagreco, L., Paciucci, M., 2008. Incised valleys, their filling and mammal fossil record - a case study from Middle-Upper Pleistocene deposits of the Roman Basin (Latium, Italy). In: Amorosi, A., Haq, B.U., Sabato, L. (Eds.), Advances in Application of Sequence Stratigraphy in Italy, vol. 1. GeoActa (Special Publication), pp. 667e687.

Nehrbass-Ahles, C., Shin, J., Schmitt, J., Bereiter, B., Joos, F., Schilt, A., Schmidely, L., Silva, L., Teste, G., Grilli, R., Chappellaz, J., Hodell, D., Fischer, H., Stocker, 2020. Abrupt CO_2 release to the atmosphere under both glacial and early interglacial conditions. Science 369, 1000e1005.

Niespolo, E.M., Rutte, D., Deino, A.L., Renne, P.R., 2017. Intercalibration and age of the Alder Creek sanidine 40Ar/39Ar standard. Quat. Geochronol. 39, 205e213.

Nomade, S., Gauthier, A., Guillou, H., Pastre, J.F., 2010. 40Ar/39Ar temporal framework for the Alleret maar lacustrine sequence (French Massif-Central): volcanological and paleoclimatic implications. Quat. Geochronol. 5, 20e27.

Nomade, S., Muttoni, G., Guillou, H., Robin, E., Scardia, G., 2011. First $^{40}Ar/^{39}Ar$ age of the Ceprano man (central Italy). Quat. Geochronol. 6, 453e457.

Paillard, D., 2001. Glacial cycles: Toward a new paradigm. Rev. Geophys. 39, 325e46.

Patacca, E., Sartori, R., Scandone, P., 1990. Tyrrhenian basin and apenninic arcs: kinematic relations since late Tortonian times. Memor. Soc. Geol. Ital. 45, 425e451.

Pereira, A., Monaco, L., Marra, F., Nomade, S., Gaeta, M., Leicher, N., Palladino, D.M., Sottili, G., Guillou, H., Scao, V., Giaccio, B., 2020. Tephrochronology of the central Mediterranean MIS 11c interglacial (~425-395 ka): new constraints from Vico volcano and Tiber delta, Central Italy. Quat. Sci. Rev. 243, 106470.

Raymo, M., Mitrovica, J., 2012. Collapse of polar ice sheets during the stage 11 interglacial. Nature 483, 453e456. https://doi.org/10.1038/nature10891.

Renne, P.R., Mundil, R., Balco, G., Min, K., Ludwig, K.R., 2010. Joint determination of 40K decay constants and 40Ar*/40K for the Fish Canyon sanidine standard, and improved accuracy for 40Ar/39Ar geochronology. Geochem. Cosmochim. Acta 74, 5349e5367.

Renne, P.R., Mundil, L.R., Balco, G., Min, K., et Ludwig, K.R., 2011. Joint determination of 40K decay constants and 40Ar*/40K for the Fish Canyon sanidine standard, and improved accuracy for 40Ar/39Ar geochronology. Response to the comment by W.H. Schwarz et al. Geochem. Cosmochim. Acta 75, 5097e5100.

Rodrigues, T., Voelker, A.H.L., Grimalt, J.O., Abrantes, F., Naughton, F., 2011. Iberian Margin sea surface temperature during MIS 15 to 9 (580e300 ka): glacial suborbital variability versus interglacial stability. Paleoceanography 26, PA1204.

Rohling, E.J., Marsh, R., Wells, N.C., Siddall, M., Edwards, N.R., 2004. Similar melt-water contributions to glacial sea level changes from Antarctic and northern ice sheets. Nature 430, 1016e1021.

Rohling, E.J., Grant, K., Bolshaw, M., Roberts, A.P., Siddall, M., Hemleben, C., Kucera, M., 2009. Antarctic temperature and global sea level closely coupled over the past five glacial cycles. Nat. Geosci. 2, 500e504.

Rohling, E.J., Fenton, M., Jorissen, F.J., Bertrand, P., Ganssen, G., Caulet, J.P., 1998. Magnitudes of sea-level low stands of the past 500,000 years. Nature 394, 162e165.

Rohling, E.J., Foster, G.L., Grant, K.M., Marino, G., Roberts, A.P., Tamisiea, M.E., Williams, F., 2014. Sea-level and deep-sea-temperature variability over the past 5.3 million years. Nature 508, 477e482.

Rohling, E.J., Hibbert, F.D., Grant, K.M., Galaasen, E.V., Irvali, N., Kleiven, H.F., Marino, G., Ninnemann, U., Roberts, A.P., Rosenthal, Y., 2019. Asynchronous Antarctic and Greenland ice-volume contributions to the last interglacial sea-level highstand. Nat. Commun. 10, 5040.

Rohling, E.J., Hibbert, F.D., Williams, F.H., Grant, K.M., Marino, G., Foster, G.L., Hennekam, R., de Lange, G.J., Roberts, A.P., Yu, J., Webster, J.M., Yokoyama, Y., 2017. Differences between the last two glacial maxima and implications for ice-sheet, $\delta^{18}O$, and sea-level reconstructions. Quat. Sci. Rev. 176, 1e28.

Rohling, E.J., Marino, G., Foster, G.L., Goodwin, P.A., von der Heydt, A.S., Köhler, P., 2018. Comparing climate sensitivity. Past and present. Annual Review of Marine Science 10, 261e288.

Shackleton, N.J., Hall, M.A., Vincent, E., 2000. Phase relationships between millennial-scale events 64,000e24,000 years ago. Paleoceanography 15,

565e569.
Siddall, M., Rohling, E.J., Almogi-Labin, A., Hemleben, C., Meischner, D., Schmelzer, I., Smeed, D.A., 2003. Sea-level fluctuations during the last glacial cycle. Nature 423, 853e858.
Sottili, G., Palladino, D.M., Marra, F., Jicha, B., Karner, D.B., Renne, P.R., 2010. Geochronology of the most recent activity in the Sabatini volcanic district, roman province, central Italy. J. Volcanol. Geoth. Res. 196, 20e30. https://doi.org/10.1016/j.jvolgeores.2010.07.003.
Stocker, T.F., Johnsen, S.J., 2003. A minimum thermodynamic model for the bipolar seesaw. Paleoceanography 18, 1087.
Wagner, B., Vogel, H., Francke, A., Friedrich, T., Donders, T., Lacey, J.H., Leng, M.J., Regattieri, E., Sadori, L., Wilke, T., Zanchetta, G., Albrecht, C., Bertini, A., Combourieu-Nebout, N., Cvetkoska, A., Giaccio, B., Grazhdani, A., Hauffe, T., Holtvoeth, J., Joannin, S., Jovanovska, E., Just, J., Kouli, K., Kousis, I., Koutsodendris, A., Krastel, S., Lagos, M., Leicher, N., Levkov, Z., Lindhorst, K., Masi, A., Melles, M., Mercuri, A.M., Nomade, S., Nowaczyk, N., Panagiotopoulos, K., Peyron, O., Reed, J.M., Sagnotti, L., Sinopoli, G., Stelbrink, B., Sulpizio, R., Timmermann, A., Tofilovska, S., Torri, P., Wagner-Cremer, F., Wonik, T., Zhang, X., 2019. Mediterranean winter rainfall in phase with African monsoons during the past 1.36 million years. Nature 573, 156e260.
Weber, M.E., Clark, P.U., Kuhn, G., Timmermann, A., Sprenk, D., Gladstone, R., Zhang, X., Lohmann, G., Menviel, L., Chikamoto, M.O., Friedrich, T., Ohlwein, C., 2014. Millenial-scale variability in Antarctic ice-sheet discharge during the last deglaciation. Nature 510, 134e138.